nature nanotechnology

ARTICLES

PUBLISHED ONLINE: 23 OCTOBER 2011 | DOI: 10.1038/NNANO.2011.166

Accumulation of sub-100 nm polymeric micelles in poorly permeable tumours depends on size

H. Cabral[1], Y. Matsumoto[2], K. Mizuno[3], Q. Chen[4], M. Murakami[2], M. Kimura[2], Y. Terada[5], M. R. Kano[6], K. Miyazono[6,7], M. Uesaka[3,7], N. Nishiyama[2,7]* and K. Kataoka[1,2,4,7]*

A major goal in cancer research is to develop carriers that can deliver drugs effectively and without side effects. Liposomal and particulate carriers with diameters of ~100 nm have been widely used to improve the distribution and tumour accumulation of cancer drugs, but so far they have only been effective for treating highly permeable tumours. Here, we compare the accumulation and effectiveness of different sizes of long-circulating, drug-loaded polymeric micelles (with diameters of 30, 50, 70 and 100 nm) in both highly and poorly permeable tumours. All the polymer micelles penetrated highly permeable tumours in mice, but only the 30 nm micelles could penetrate poorly permeable pancreatic tumours to achieve an antitumour effect. We also showed that the penetration and efficacy of the larger micelles could be enhanced by using a transforming growth factor-β inhibitor to increase the permeability of the tumours.

Targeting tumours with long-circulating nanomedicines, such as poly(ethylene glycol)-modified liposomes and polymeric micelles[1–6], is a promising strategy in systemic cancer treatment. These materials accumulate in solid tumours through the enhanced permeability and retention (EPR) effect[7], which is characterized by leaky blood vessels and an impaired lymphatic drainage in tumour tissues[7]. Compared with free drug, nanomedicines accumulate in solid tumours more easily and selectively and therefore offer better antitumour activity[8–15]. Several nanomedicines, including Doxil and Abraxane (diameters of 90 and 130 nm, respectively), have shown significant antitumour activity in highly vascularized tumours such as Kaposi's sarcoma and breast cancer, and have been approved for clinical use[16,17]. However, because Doxil and other nanomedicines with diameters larger than 100 nm have shown limited penetration and accumulation in tumours with hypovascular and hypopermeable characteristics[18–20] (such as intractable pancreatic tumours[18,20]), nanomedicines in the sub-100 nm range are now regarded as being more important in the study of tumour penetration[21,22].

Polymeric micelles (self-assemblies of block copolymers) are promising long-circulating nanomedicines[5,6,8–10] and have been widely studied in preclinical and clinical trials[13,14,23]. Clinical studies have demonstrated that polymeric micelles of poly(ethylene glycol)–*b*-poly(amino acid) copolymers incorporating paclitaxel, SN-38, doxorubicin or cisplatin drugs can reduce the toxic side effects of the loaded drugs[13,14,24,25] while maintaining appreciable antitumour efficacy. Micelles containing paclitaxel and SN-38 have been reported to reduce the size of tumours in patients with advanced cancers of the breast and pancreas[13,14]. The dense poly(ethylene glycol) (PEG) shell of the micelles prevents protein adsorption and recognition by the phagocyte system, and this prolongs blood circulation, a prerequisite for enhanced tumour accumulation based on the EPR effect. Moreover, with these micelles, the size (including those in the sub-100 nm range), stability, loading capacity and release kinetics of the drugs can be modulated by engineering the constituent block copolymers[5,6]. Here, we examine whether a series of micellar nanomedicines that have diameters less than 100 nm and that carry the potent tumoricidal agent 1,2-diaminocyclohexane-platinum(II) (DACHPt) (the parent complex of oxaliplatin) can accumulate and penetrate poorly permeable pancreatic tumours. Our results show that the size of the nanomedicines critically affects the penetration and efficacy of the drugs in the tumours. Larger micelles that could not penetrate otherwise, could penetrate once the permeability of the tumours was improved by administering a transforming growth factor-β inhibitor.

Characterization of DACHPt-loaded micelles

DACHPt-loaded micelles (DACHPt/m) were spontaneously formed from the interaction of the platinum of DACHPt and the carboxylic moieties of PEG–*b*-poly(glutamic acid) (PEG–*b*-P(Glu)) copolymer and the poly(glutamic acid) (P(Glu)) homopolymer in water (Fig. 1a)[10,26,27]. Differently sized DACHPt/m were synthesized by controlling the mixing ratio of P(Glu) from the homopolymer and the P(Glu) portion of PEG–*b*-P(Glu) (Fig. 1b). As the ratio of P(Glu) in the homopolymer and P(Glu) in the copolymer increases, the size of the micelles increases. Thus, the size of DACHPt/m ranged from 30 nm without the addition of P(Glu) homopolymer to more than 100 nm, while maintaining a narrow distribution as determined by dynamic light scattering (DLS) measurements and transmission electron microscopy (TEM) observations (Table 1 and Supplementary Fig. S1, respectively). Note that DLS measurements provide the hydrodynamic diameter of the DACHPt/m, and TEM gives the core diameter of the micelles, so the difference between the hydrodynamic diameter and the core size gives an indication of the thickness of the PEG shell of the micelles.

[1]Department of Bioengineering, Graduate School of Engineering, The University of Tokyo, 7-3-1 Hongo, Bunkyo-ku, Tokyo, 113-8656, Japan, [2]Center for Disease Biology and Integrative Medicine, Graduate School of Medicine, The University of Tokyo, 7-3-1 Hongo, Bunkyo-ku, Tokyo 113-0033, Japan, [3]Department of Nuclear Engineering and Management, Graduate School of Engineering, The University of Tokyo, 7-3-1 Hongo, Bunkyo-ku, Tokyo 113-8656, Japan, [4]Department of Materials Engineering, Graduate School of Engineering, The University of Tokyo, 7-3-1 Hongo, Bunkyo-ku, Tokyo 113-8656, Japan, [5]SPring 8, JASRI, 1-1-1 Kouto, Sayo-cho, Sayo-gun, Hyogo 679-5198, Japan, [6]Department of Molecular Pathology, Graduate School of Medicine, The University of Tokyo, 7-3-1 Hongo, Bunkyo-ku, Tokyo 113-0033, Japan, [7]Center for NanoBio Integration (CNBI), The University of Tokyo, 7-3-1 Hongo, Bunkyo-ku, Tokyo 113-8656, Japan. *e-mail: nishiyama@bmw.t.u-tokyo.ac.jp; kataoka@bmw.t.u-tokyo.ac.jp

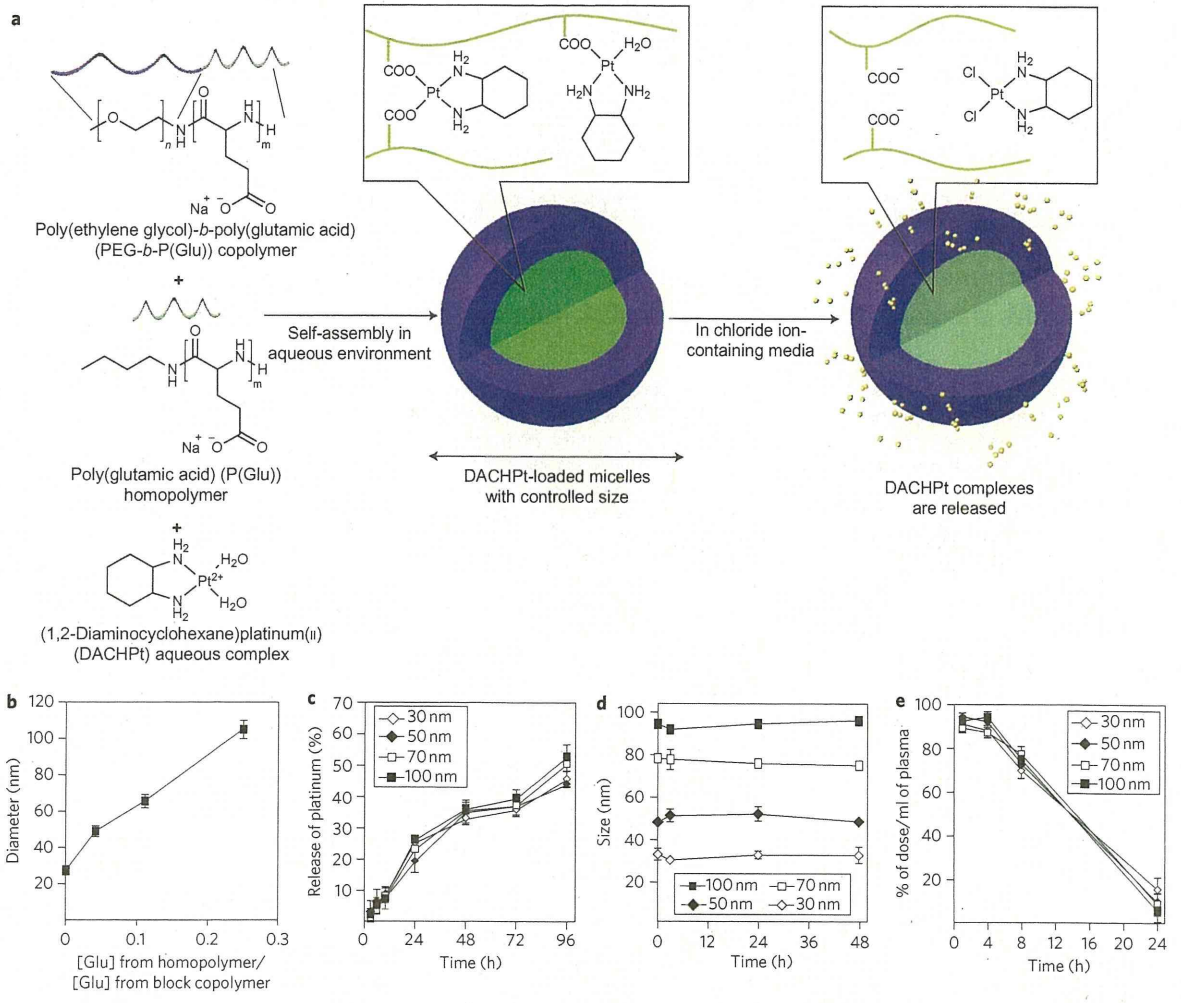

Figure 1 | Construction and physicochemical properties of DACHPt-loaded micellar nanomedicines (DACHPt/m) with different diameters. a, Schematic showing DACHPt/m formed through the interaction between DACHPt and the carboxylic groups of poly(glutamic acid) (green) in PEG-*b*-P(Glu) and P(Glu). In media containing chloride ions, DACHPt (yellow circles) is released from the micelles through ligand exchange between the carboxylic groups in P(Glu) and the chloride ions. **b**, Changing micelle size by altering the ratio of P(Glu) from the homopolymer and the P(Glu) portion of PEG-*b*-P(Glu) in the mixture. Total glutamic acid residue concentration was maintained at 5 mM. **c**, Micelles of all sizes release DACHPt at similar rates. **d**, Micelles of all sizes incubated in cell culture media containing 10% serum at 37 °C maintained their sizes over 48 h. **e**, Plasma clearances of micelles with different diameters follow similar trends. Data are means ± s.e.m., $n = 3$.

Table 1 | Diameter, size distribution, drug loading and surface charge of 30, 50, 70 and 100 nm micelles.

Size (nm)*	Polydispersity index	[Pt]/[COO] (mol/mol)†	Pt/polymer (wt/wt%)	Zeta-potential (mV)‡
30	0.16	0.56	34	−2.29 ± 1.41
54	0.14	0.6	48	−1.61 ± 0.58
69	0.12	0.57	54	−0.89 ± 0.33
110	0.11	0.52	69	0.15 ± 0.21

*Determined by DLS. †Determined by ICP-MS (platinum concentration) and weight of micelles. ‡Determined by laser doppler electrophoresis ($n = 4$, mean ± s.d.).

The 30, 50, 70 and 100 nm DACHPt/m presented similar zeta potentials, ranging from −2.29 to 0.15 mV at pH 7.4 (Table 1). These micelles showed similar drug release rates (Fig. 1c), driven by the ligand exchange of DACHPt between the carboxylic groups of P(Glu) and the chloride ions in the biological media. After 96 h incubation in cell culture media containing 10% fetal bovine serum (FBS) at 37 °C, the drug release from DACHPt/m reached ~50% (Fig. 1c). Under similar conditions, differently sized DACHPt/m maintained their diameters for over 48 h (Fig. 1d). DACHPt/m of different sizes also showed similar plasma clearance rates (~12% of injected dose (ID) per ml plasma remained after 24 h) and plasma half-lives (7–8 h) (Fig. 1e and Supplementary Table S1, respectively). We recently showed that DACHPt/m can maintain their micellar structure in the circulation for at least 24 h after injection[28]. Furthermore, DACHPt/m of varying sizes show similar distributions in the kidney, liver and spleen (Supplementary Fig. S2 and

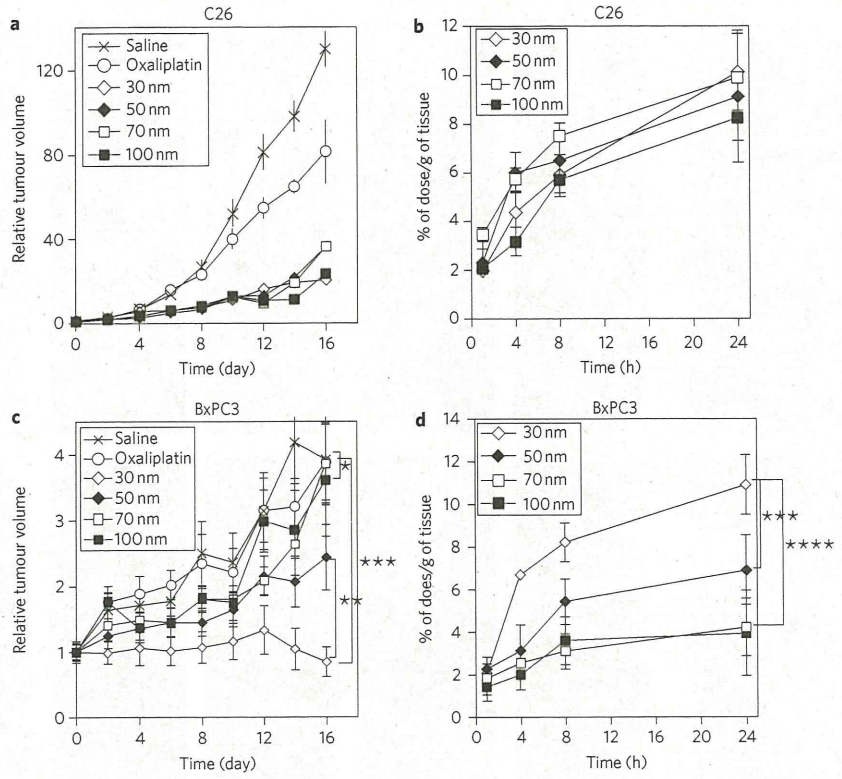

Figure 2 | Anticancer activity and tumour accumulation of DACHPt/m with different diameters. a–d, Plots of relative tumour volumes of subcutaneous hyperpermeable murine colon adenocarcinoma (C26) (**a**) and subcutaneous hypopermeable human pancreatic adenocarcinoma BxPC3 (**c**) tumours, and accumulation of DACHPt/m in C26 (**b**) and BxPC3 (**d**) tumours. To evaluate antitumour activity, oxaliplatin was injected on days 0, 2 and 4 (dose, 8 mg kg^{-1}) and micelles were injected on days 0, 2 and 4 (dose, 3 mg kg^{-1} on a platinum basis). For tumour accumulation experiments, micelles were injected at 100 μg per mouse on a platinum basis. Data are means ± s.e.m., $n = 6$. *$P > 0.05$; **$P < 0.05$; ***$P < 0.01$; ****$P < 0.001$.

Table S1), which are the major organs responsible for the clearance of nanocarriers[29]. The levels of accumulation of DACHPt/m in these organs are comparable to other polymeric micelles incorporating cisplatin[8] or doxorubicin[9], except for a slightly higher accumulation of 100 nm DACHPt/m in the liver. Because the surface chemistry and charge of nanocarriers have been reported to critically affect the interactions of nanocarriers with plasma proteins and cells and the biodistributions of nanocarriers[21,22,29,30], the analogous surface chemistry (PEG-coated surface), neutral charge and comparable plasma clearance of DACHPt/m with different diameters are substantial advantages for the evaluation of their extravasation, penetration and accumulation abilities in solid tumours as well as the associated therapeutic outcomes.

Antitumour activity of DACHPt/m in solid tumours

The antitumour activity and accumulation of DACHPt/m with different diameters were examined in tumour models with different permeabilities: a hyperpermeable murine colon adenocarcinoma 26 (C26) model characterized by high vascularization and slight tumour stroma[31] and a human pancreatic adenocarcinoma BxPC3 characterized by low vascularization, reduced vascular permeability due to pericyte coverage of blood vessels[20,31] and thick fibrosis, which are representative characteristics of some intractable solid tumours[20,31–33]. Note that the *in vitro* cytotoxicity of sub-100 nm DACHPt/m on C26 and BxPC3 cell lines was not substantially affected by micelle size (Supplementary Table S3), suggesting that their *in vivo* antitumour effect can be associated with their accumulation and microdistribution in solid tumours. In the C26 model, all micelles demonstrated comparable tumour growth inhibition (Fig. 2a), whereas oxaliplatin did not show a significant antitumour effect. The accumulation levels of all sub-100 nm micelles in C26 tumours were consistently comparable, reaching ~10% ID g^{-1} tumour at 24 h post-injection (Fig. 2b). In the BxPC3 model, the size effect of DACHPt/m on antitumour activity became evident, with the 30 nm micelles completely suppressing tumour growth, the 50 nm micelles leading to reduced antitumour activity, and the 70 nm and 100 nm micelles failing to show any antitumour effect (Fig. 2c). The accumulation of the 30 nm micelles was two times higher than that of the 50 nm micelles and four times higher than that of the 70 and 100 nm micelles after 24 h in BxPC3 tumours (Fig. 2d), which is also consistent with the antitumour efficacies in Fig. 2c.

The intratumoral microdistribution of fluorescently labelled DACHPt/m with different sizes in tumour sections was studied to investigate size-dependent extravasation and penetration of micellar nanomedicines in tumours. Histological investigations using haematoxilyn and eosin (H&E) staining revealed a well-vascularized medullary histological pattern of C26 tumours with reduced tumour stroma (Fig. 3a). In this tumour model, the fluorescence signals from the 30, 50, 70 and 100 nm micelles were uniformly distributed throughout the entire section at 24 h post-injection, suggesting deep tumour penetration of all sub-100 nm micelles (Fig. 3b, red). The immunofluorescence localization of platelet endothelial cell adhesion molecule-1 (PECAM-1), expressed by endothelial cells, indicated the extensive distribution of blood vessels in C26 tumours (Fig. 3b, green). However, H&E staining of BxPC3 tumours revealed the formation of nests of cancer cells surrounded by fibrotic tissue (Fig. 3c), which may act as a barrier

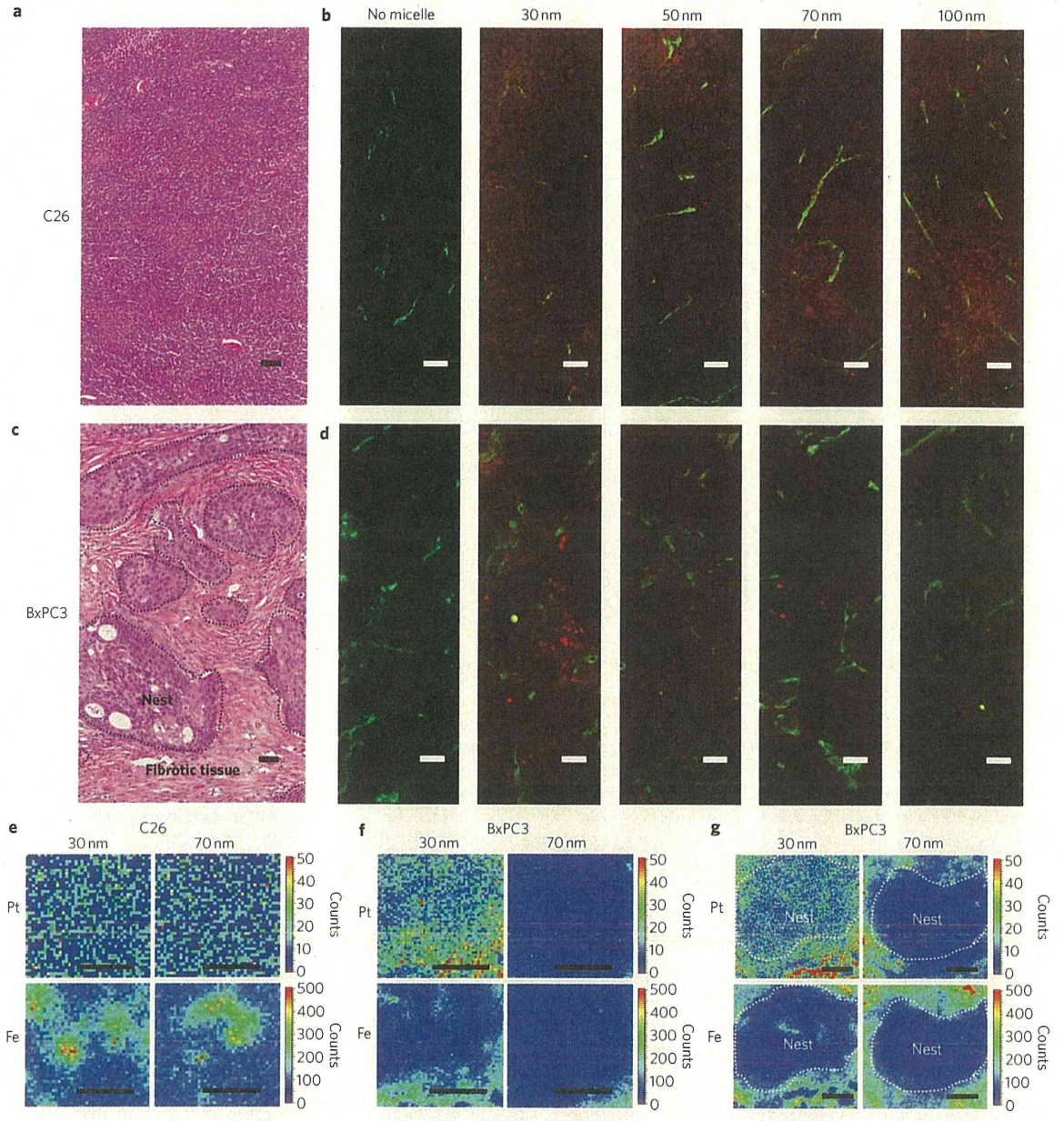

Figure 3 | Microdistribution of fluorescently labelled DACHPt/m of varying sizes in tumours. a–d, Histological examination of C26 tumour (**a**) and BxPC3 tumour (**c**) by H&E staining (dashed lines in **c** show area of cancer cell nests in the BxPC3 tumour) and fluorescent microscopic images of sections of C26 (**b**) and BxPC3 (**d**) tumours 24 h after intravenous administration of fluorescent micelles with different sizes. Micelles were labelled with Alexa 594 (red). Blood vessels were marked with PECAM-1 and Alexa 488 secondary antibody (green). Scale bars, 50 μm. **e–g**, Mapping of platinum atoms from DACHPt and iron from haemoproteins in tumour sections of C26 (**e**), BxPC3 (**f**) and a BxPC3 cancer cell nest (indicated by dashed line) (**g**) by μ-SR-XRF 24 h after administration of micelles. Scale bars, 50 μm.

against the penetration of drugs and nanocarriers[20,31]. In the BxPC3 model, immunofluorescence detection of PECAM-1 (Fig. 3d, green) indicated the presence of blood vessels around the cancer cell nests and the absence of vessels in the interior of these structures. We observed that the 30 nm micelles penetrated inside the tightly nested structures of BxPC3 tumours, but the fluorescent signal of the bigger micelles diminished and was concentrated close to the blood vessels, indicating their failure to enter the nests of cancer cells (Fig. 3d, red). This size-dependent penetration of fluorescent DACHPt/m may affect the intratumoral distribution of the delivered drug.

Given that the drug loaded in the micelles was a platinum complex, we assessed the drug microdistribution in tumour sections by detecting element disposition using μ-synchrotron radiation X-ray fluorescence (μ-SR-XRF). The very distinct peak of the platinum from the DACHPt can be observed in the sum spectrum of the line scan as well as the elements traditionally present in animal tissue. The distribution of iron and platinum in tumour tissue

sections was studied to evaluate the distribution of haemoproteins (linked to the presence of blood vessels) and the location of the drug, respectively. For this experiment, we used DACHPt/m with diameters of 30 and 70 nm because of the critical differences in antitumour activity, tumour accumulation and microdistribution of DACHPt/m in the BxPC3 tumour model for diameters below and above 50 nm (Figs 2c,d, 3d).

In the C26 tumour model, the extensive spread of iron atoms indicates abundant vascularization (Fig. 3e), consistent with the abundance of blood vessels observed by immunofluorescence microscopy (Fig. 3b, green). DACHPt delivered from the 30 and 70 nm micelles was broadly distributed in this tumour model (Fig. 3e). In the BxPC3 xenografts, the distribution of iron atoms (Fig. 3f,g) indicates reduced vascularization and disposition of blood vessels in this model, suggesting a restricted blood flow inside the nest structures. The platinum mapping shows that the 30 nm micelles delivered DACHPt inside the cancer cell nests, whereas DACHPt from the 70 nm micelles is localized in the periphery of the nests (Fig. 3g). In both tumour models, the intratumoral microdistribution of DACHPt has a layout similar to that of the fluorescent micelles, confirming that tumour penetration by the micelles directly affects drug accumulation and antitumour outcome.

The real-time observation of *in vivo* behaviour of nanocarriers might reveal the critical barriers in a living body. Unlike conventional histological analysis, the *in vivo* confocal laser scanning microscopy (CLSM) technique enables spatiotemporal and quantitative analyses of extravasation, tissue penetration and cellular internalization of nanocarriers in a living animal[34]. By using an *in vivo* CLSM combined with a high-speed resonance scanner designed to acquire clean live tissue images, we intravitally evaluated the penetration and accumulation of the fluorescently labelled micelles. The 30 and 70 nm micelles were labelled with Alexa 488 (green) and Alexa 594 (red) fluorescent probes, respectively (Supplementary Fig. S3), and concurrently injected into tumour-bearing mice to evaluate real-time extravasation, penetration and microdistribution of both micelles in the same tumour (Fig. 4). Fluorescence measurements in the tissues were relative to the fluorescence intensity in the vasculature immediately after injection of the micelles (V_{max}).

At 1 h post-injection of the micelles, the fluorescence intensity of both 30 and 70 nm DACHPt/m in the blood vessels of tumours was ~80% of V_{max} (Fig. 4a,b). In C26 tumours, the micelles showed similar extravasation and penetration (Fig. 4a, Supplementary Video S1). The z-stack volume reconstruction of the C26 tumour showed a profusely vascularized structure and a comparable presence of both micelles in the tumour interstitium (Fig. 4c, Supplementary Video S2). In BxPC3 tumours, the extravasation profiles of the 30 and 70 nm micelles after 1 h were clearly dissimilar (Fig. 4b, Supplementary Videos S3, S4). The 30 nm micelles crossed the vascular wall, achieving over 20% of V_{max} at 40 μm from the blood vessel (Fig. 4b). In contrast, the 70 nm micelles extravasated at discrete sites close to the blood vessels and failed to move towards the interstitial space (Fig. 4b). These distinct penetration profiles were evident in the z-stack volume reconstruction of the BxPC3 tumour, showing that the extravasation points of the 70 nm micelles surrounded the blood vessels (Fig. 4d,e, Supplementary Videos S5 and S6). At 24 h post-injection, the intensities of the extravasated 30 and 70 nm micelles in the C26 tumour were ~40% of V_{max} at 100 μm from the blood vessels (Fig. 4f), and both micelles were observed inside the individual cells of the tumour tissue (Fig. 4f). In BxPC3 tumours, the distribution of the micelles corresponded reasonably to their different extravasation profiles; the 30 nm micelles achieved deep tumour accumulation, but the 70 nm micelles remained close to the vasculature (Fig. 4g, white arrows). The intensity of the extravasated 30 nm micelles was ~40% of V_{max} (Fig. 4g) and they apparently localized in the cells (Fig. 4g). These observations strongly suggest that 30 nm DACHPt/m can penetrate nests of cancer cells distant from blood vessels, allowing homogeneous drug distribution in hypopermeable tumours.

Although many factors (including morphology, hydrophobicity and nanoparticle charge) affect their accumulation in tumours, it is of primary importance to study long-circulating nanocarriers, because prolonged circulation is a prerequisite for tumour targeting based on the EPR effect. Results obtained by intratumoral microdistribution studies indicate that micellar nanomedicines with diameters less than 50 nm might be superior in terms of extravasation and penetration into tumour tissues among the sub-100 nm micellar nanomedicines. The limitation of the present study is that the size of the micellar nanomedicines was restricted to between 30 and 100 nm. Because the threshold of renal clearance of nanoparticles is ~5.5 nm (ref. 35), tumour accumulation and intratumoral distribution of nanomedicines in the range between 5 and 30 nm remain to be clarified. Furthermore, the biodistribution study revealed that the 100 nm micelles showed higher accumulation in the liver compared with other smaller micelles (Supplementary Fig. S2, Table S1), suggesting the importance of the size of nanomedicines for their distribution in organs, which may be associated with toxicity. Hence, optimizing the size of nanomedicines should take into account the balance between antitumour efficacy and potential toxicity.

Enhancing tumour permeability with a TGF-β inhibitor

We have recently reported that low doses of a transforming growth factor (TGF)-β inhibitor (TGF-β-I) transiently decreases the pericyte coverage of the endothelium in the neovasculature of pancreatic tumours, resulting in enhanced accumulation and antitumour activity of 65 nm micellar nanomedicines and 90 nm Doxil[20]. These results motivated us to evaluate the effect of the TGF-β inhibitor on the delivery of sub-100 nm DACHPt/m in BxPC3 tumours. When mice were treated with 1 mg kg^{-1} of TGF-β-I (LY364947), the 70 nm micelles reduced the tumour growth rate as effectively as the 30 nm micelles (Fig. 5a). Moreover, accumulation of the 70 nm micelles in tumours was augmented to a level comparable with that of the 30 nm micelles (Fig. 5b). These results indicate that the impaired extravasation and penetration of the 70 nm micelles in BxPC3 tumours can be overcome by treatment with TGF-β-I.

Fluorescence microscopic evaluation of BxPC3 tumour sections revealed that the fluorescently labelled 70 nm micelles showed enhanced intratumoural penetration even inside cancer cell nests after administration of TGF-β-I (Fig. 5c). This result suggests that modulation of the stromal components in tumour tissue by TGF-β-I, including pericyte coverage around the tumour blood vessels, is important for penetration of the 70 nm micelles. Moreover, the μ-SR-XRF measurement demonstrated that co-administration of TGF-β-I facilitated intratumoral delivery of DACHPt from the 70 nm micelles, which reached the interior of the cancer cell nests at 24 h post-injection (Fig. 5d). This result is consistent with the augmented antitumour activity (Fig. 5a) and enhanced intratumoural penetration (Fig. 5b) of 70 nm DACHPt/m by TGF-β-I.

Intravital CLSM observation also confirmed that treatment with TGF-β-I enhanced the extravasation and penetration of 70 nm micelles into BxPC3 tumours (Fig. 5e, Supplementary Video S7). We found that the 30 and 70 nm micelles demonstrated a comparable distribution in the tumour tissues, and both achieved ~20% of V_{max} at 40 μm from the blood vessels at 1 h after co-injection (Fig. 5e). At 24 h after injection, both micelles had deeply penetrated the tumour (Fig. 5f), reaching over 40% of V_{max} at 100 μm from the blood vessels (Fig. 5f). The 30 and 70 nm micelles also appeared to show comparable subcellular localization (Fig. 5f). These results suggest that the improvement in extravasation and penetration of 70 nm DACHPt/m by TGF-β-I caused the increased antitumour

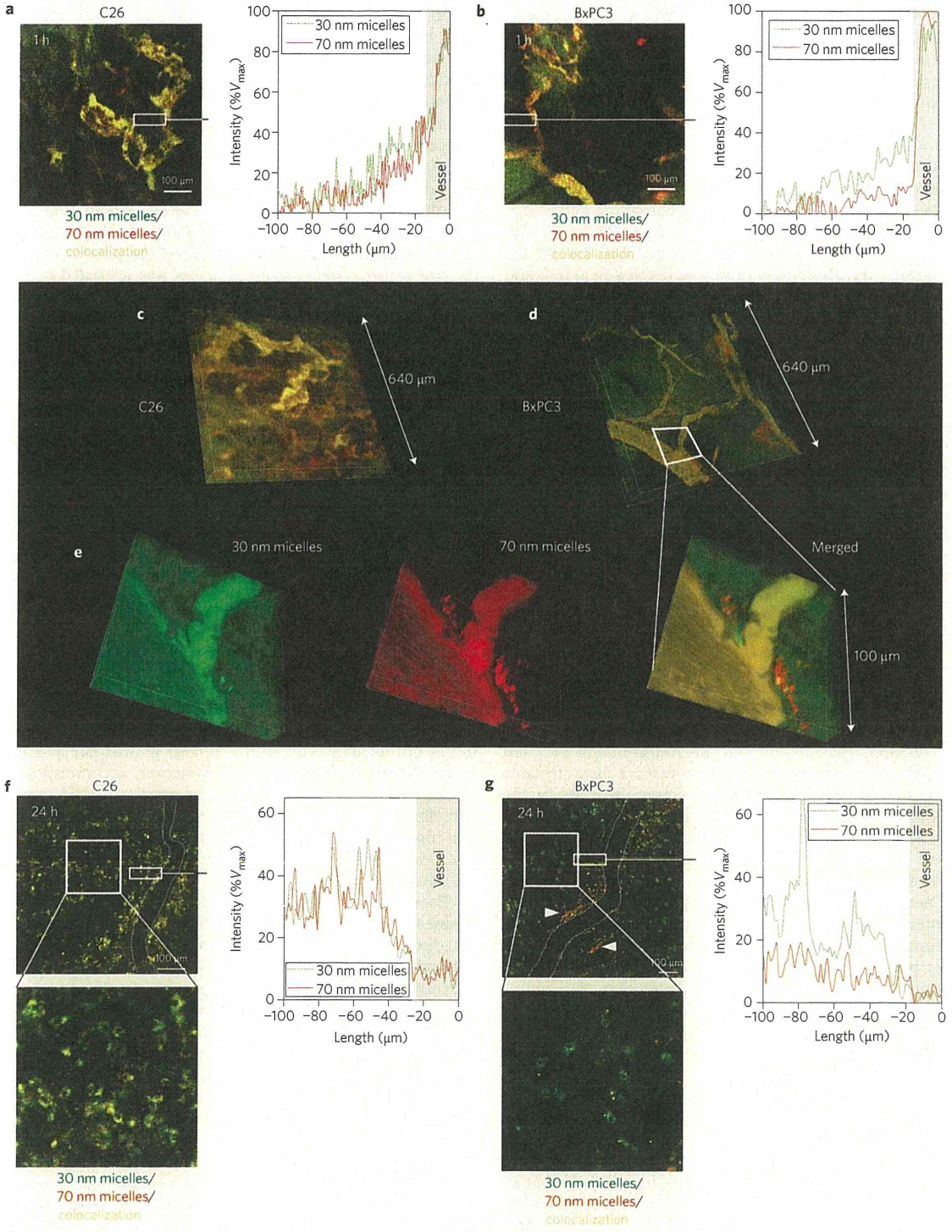

Figure 4 | *In vivo* real-time microdistribution of DACHPt/m with different diameters in tumours. a,b, Microdistribution of fluorescently labelled 30 nm (green) and 70 nm (red) micelles 1 h after injection into C26 (**a**) and BxPC3 (**b**) tumours. Their colocalization is shown in yellow. Right panels in **a** and **b** show fluorescence intensity profile from the blood vessel (0–10 μm; grey area) to the tumour tissue (10–100 μm) in the selected region (indicated by a white rectangle) expressed as a percentage of the maximum fluorescence intensity attained in the vascular region (%V_{max}). **c,d**, Z-stack volume reconstruction of C26 (**c**) and BxPC3 (**d**) tumours 1 h after co-injection of the fluorescent micelles. **e**, Magnification of the perivascular region (indicated by a white trapezium) of the z-stack volume image of BxPC3 tumours. **f,g**, Distribution of 30 and 70 nm micelles 24 h after injection into C26 tumours (**f**) and BxPC3 tumours (**g**). White arrows in **g** indicate 70 nm micelles localizing at perivascular regions. Right panels show fluorescence intensity profile from the blood vessel (0–10 μm; grey area) to the tumour tissue (10–100 μm) in the selected region (indicated by white rectangle).

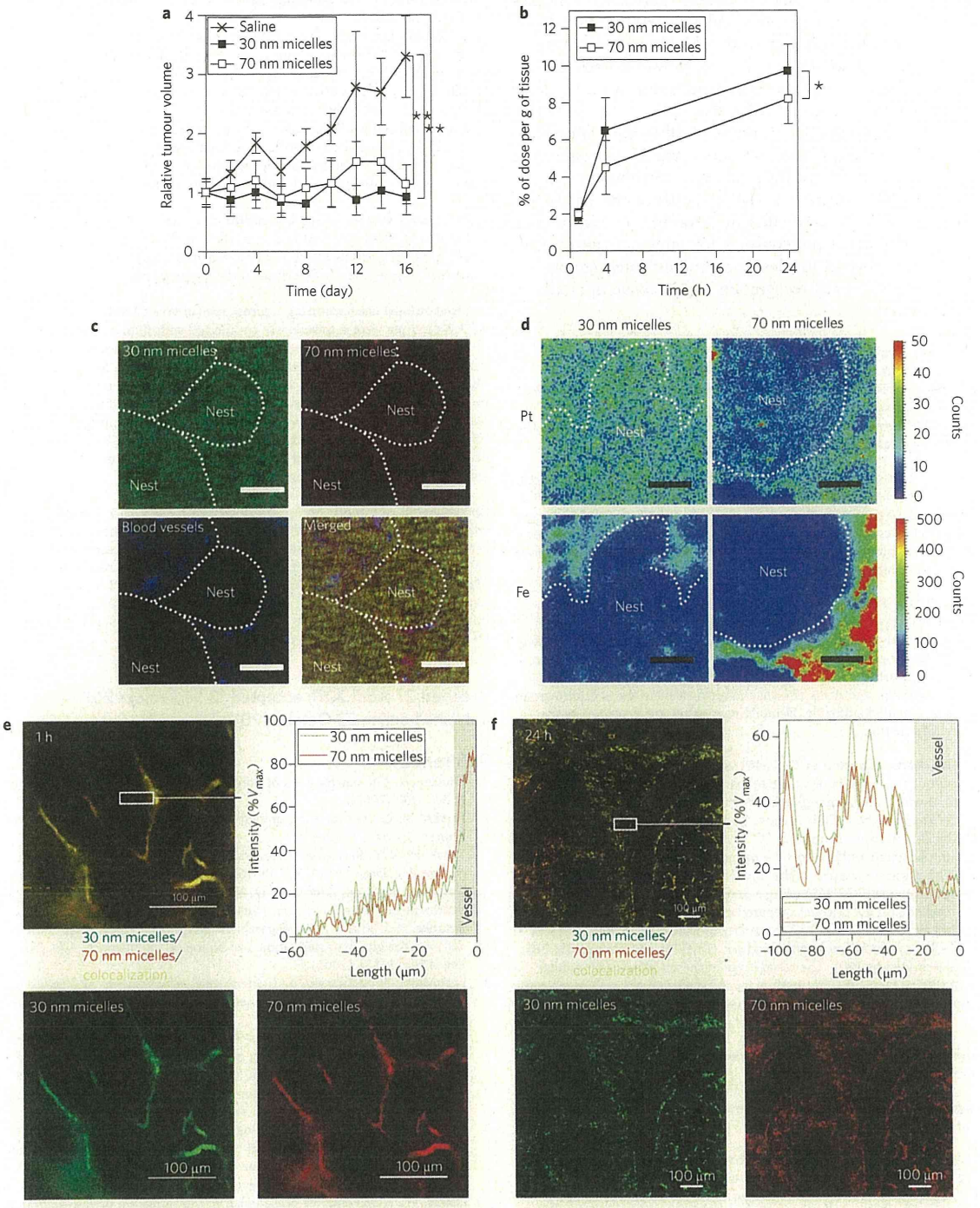

Figure 5 | Effect of TGF-β inhibitor (TGF-β-I) on antitumour activity and tumour accumulation of DACHPt/m in BxPC3 tumours. a, Graph showing relative tumour volume. Micelles (3 mg kg^{-1}) were injected on days 0, 4 and 8 and TGF-β-I on days 0, 2, 4, 6 and 8. **b**, Graph showing accumulation of 30 and 70 nm DACHPt/m in BxPC3 tumours after injection of TGF-β-I. Data are expressed as means ± s.e.m., $n = 6$. *$P > 0.05$; **$P < 0.01$. **c**, Fluorescent microscopy of tumour sections 24 h after co-administration of the fluorescent micelles and TGF-β-I. Scale bars, 50 μm. **d**, Platinum and iron mapping of tumour sections by μ-SR-XRF 24 h after administration of 30 and 70 nm micelles. Scale bars, 50 μm. **e**,**f**, Intravital distribution of 30 nm (green) and 70 nm (red) micelles in BxPC3 tumours 1 h (**e**) and 24 h (**f**) after co-injection of micelles and TGF-β-I. Their colocalization is shown in yellow. Right panels show fluorescence intensity profile from the blood vessel (grey area) to the tumour tissue in the selected region (indicated by a white rectangle).

activity, supporting the hypothesis that TGF-β inhibitors have great potential for enhancing the therapeutic efficacy of nanomedicines in hypopermeable tumours.

Conclusions

The enhanced targeting of drugs to cancer cells within tumours by nanomedicines largely depends on size. We have shown that the

tumoricidal efficiency of long-circulating polymeric micelles depends on the size of the micelles and the permeability of the tumour. In hypervascular tumours with a highly permeable structure, sub-100 nm micellar nanomedicines showed no size-dependent restrictions on extravasation and penetration in tumours. In contrast, only nanomedicines smaller than 50 nm can penetrate poorly permeable hypovascular tumours. Furthermore, increasing the permeability of hypovascular tumours using TGF-β signalling inhibitor improved the accumulation and distribution of the larger 70 nm micelles, offering a way to enhance the efficacy of larger nanomedicines. Because efficient extravasation and tumour penetration are important prerequisites for targeting cancer cells, our findings are important for designing sophisticated nanomedicines that are capable of cell recognition and selective intracellular release of payloads.

Materials and methods

Materials, cell lines and animals. Information regarding materials, cell lines (murine colon adenocarcinoma 26 (C26) cells and human pancreatic cancer BxPC3 cells) and animals is described in the Supplementary Information. All animal experiments were performed in accordance with the Guidelines for the Care and Use of Laboratory Animals as stated by the University of Tokyo.

Tumour models. BALB/c nude mice were inoculated subcutaneously with C26 cells (1×10^6 cell ml^{-1}) to prepare the hyperpermeable tumour model, or with BxPC3 cells (1×10^7 cell ml^{-1}) to prepare the hypopermeable tumour model. *In vivo* and *ex vivo* confocal microscopy, elemental mapping and antitumour activity studies were performed when tumours were 50 mm in volume[3]. Biodistribution studies were performed when the tumours were ~100 mm in volume[3].

Preparation of PEG-*b*-P(Glu) block copolymer and P(Glu) homopolymer. PEG-*b*-P(Glu) block copolymers and P(Glu) homopolymers were synthesized according to a previously described synthetic method[8] with a minor modification. Detailed procedures for polymer synthesis and characterization are described in the Supplementary Information. PEG-*b*-P(Glu) was fluorescently labelled by conjugating the Alexa 488 and Alexa 594 succinimidyl esters to the ω-amino group of the polymer in dimethyl sulfoxide. Detailed procedures are described in the Supplementary Information.

Preparation and characterization of DACHPt/m with different diameters. DACHPt/m with different diameters were prepared according to a previously described method with a slight modification[10,26,27]. Detailed procedures are described in the Supplementary Information. The size distribution of DACHPt/m was evaluated by DLS measurements at 25 °C, and the zeta potential of the micelles was measured in phosphate buffer at pH 7.4 using a Zetasizer Nano ZS90 (Malvern Instruments). The platinum content in the micelles was determined by ion-coupled plasma-mass spectrometry (ICP-MS) using a Hewlett Packard 4500 ICP-MS. Fluorescently labelled DACHPt/m was prepared in a similar manner with Alexa 488 or Alexa 594 labelled PEG-*b*-P(Glu). The stability of DACHPt/m with different diameters in Dulbecco's modified Eagle's medium (DMEM) containing 10% FBS at 37 °C was determined by DLS. The release rate of the micelles under similar conditions was studied by the dialysis method using a dialysis bag (molecular weight cutoff = 2,000). More detailed information is described in the Supplementary Information.

Transmission electron microscopy. The experimental procedure is described in the Supplementary Information.

***In vitro* cytotoxicity assay.** The experimental procedure is described in the Supplementary Information.

Antitumour activity assay. Mice were treated three times intravenously at two-day intervals with 3 mg kg^{-1} (on a platinum basis) of 30, 50, 70 and 100 nm DACHPt/m. Anti-tumour activity was evaluated in terms of tumour size (V), which was estimated by the equation

$$V = a \times b^2/2$$

where a and b are the major and minor axes of the tumour, respectively, as measured by a caliper. The statistical significance of different findings between the experimental and control groups was determined by analysis of variance (ANOVA) with Tukey's multiple comparison test. The results were considered statistically significant if two-tailed P-values were less than 0.05.

Plasma clearance and organ and tumour accumulation of DACHPt/m with different diameters. The experimental procedure is described in the Supplementary Information.

Microdistribution and immunohistochemistry of fluorescently labelled DACHPt/m. Mice bearing C26 or BxPC3 tumours were intravenously injected with Alexa 594-labelled 30, 50, 70 and 100 nm DACHPt/m at 100 μg per mouse on a platinum basis. Twenty-four hours later, tumours were collected and immediately frozen in an acetone/dry ice mixture. The frozen samples were further sectioned (thickness, 16 μm) in a cryostat, briefly fixed with cold acetone and then incubated with PECAM-1 antibody. Alexa 488 was used as the secondary antibody. Samples were observed using a Zeiss LSM510 Meta confocal microscope (Oberkochen). For H&E staining, the excised samples were fixed overnight in 4% paraformaldehyde and then paraffin-embedded to prepare them for the perfusion study in the tumour tissues. Samples were observed under an AX80 microscope (Olympus).

Element array analysis using μ-X-ray fluorescence. SR-XRF was used to determine DACHPt as well as iron distribution in sections of solid tumours (C26 or BxPC3) at 24 h post-intravenous injection of 30 and 70 nm DACHPt/m[36]. The detailed experimental procedure is described in the Supplementary Information.

***In vivo* confocal laser scanning microscopy (*in vivo* CLSM).** Mice bearing C26 or BxPC3 tumours were intravenously co-injected with fluorescently labelled 30 and 70 nm DACHPt/m at a dose of 10 mg kg^{-1}. The 30 nm micelles were labelled with Alexa 488, and the 70 nm micelles were labelled with Alexa 594. The *in vivo* CLSM observation of tumour tissues was performed according to a previously reported method[28,34]. All *in vivo* picture acquisitions were performed using a Nikon A1R confocal laser scanning microscope system attached to an upright ECLIPSE FN1 (Nikon). The 30-nm-diameter micelles were detected using 488/510 nm excitation/emission filters, and the signal from the 70 nm micelles was acquired with 560/620 nm excitation/emission filters.

Enhancement of tumour permeability by treatment with a TGF-β inhibitor. The effect of TGF-β inhibitor on the accumulation and antitumour activity of DACHPt/m was determined using the methods already described. For the antitumour activity experiment, BxPC3-bearing mice were administered intraperitoneal injections of TGF-β inhibitor LY364947 at 1 mg kg^{-1} every second day. For tumour accumulation studies, BxPC3-bearing mice received an intraperitoneal injection of the TGF-β inhibitor at 1 mg kg^{-1} at 1 h before co-injection of the 30 and 70 nm micelles.

Received 27 April 2011; accepted 12 September 2011; published online 23 October 2011

References

1. Duncan, R. The dawning era of polymer therapeutics. *Nature Rev. Drug Discov.* **2,** 347–360 (2003).
2. Ferrari, M. Cancer nanotechnology: opportunities and challenges. *Nature Rev. Cancer.* **5,** 161–171 (2005).
3. Torchilin, V. P. Recent advances with liposomes as pharmaceutical carriers. *Nature Rev. Drug Discov.* **4,** 145–160 (2005).
4. Davis, M. E., Chen, Z. & Shin, D. Nanoparticle therapeutics: an emerging treatment modality for cancer. *Nature Rev. Drug Discov.* **7,** 771–782 (2008).
5. Kataoka, K., Harada, A. & Nagasaki, Y. Block copolymer micelles for drug delivery: design, characterization and biological significance. *Adv. Drug Deliv. Rev.* **47,** 113–131 (2001).
6. Nishiyama, N. & Kataoka, K. Current state, achievements, and future prospects of polymeric micelles as nanocarriers for drug and gene delivery. *Pharmacol Ther.* **112,** 630–648 (2006).
7. Matsumura, Y. & Maeda, H. A new concept for macromolecular therapeutics in cancer chemotherapy: mechanism of tumouritropic accumulation of proteins and the antitumour agent SMANCS. *Cancer Res.* **46,** 6387–6392 (1986).
8. Nishiyama, N. *et al.* Novel cisplatin-incorporated polymeric micelles can eradicate solid tumours in mice. *Cancer Res.* **63,** 8977–8983 (2003).
9. Bae, Y. *et al.* Preparation and biological characterization of polymeric micelle drug carriers with intracellular pH-triggered drug release property: tumor permeability, controlled subcellular drug distribution, and enhanced *in vivo* antitumor efficacy. *Bioconjug. Chem.* **16,** 122–130 (2005).
10. Cabral, H., Nishiyama, N. & Kataoka, K. Optimization of (1,2-diamino-cyclohexane) platinum(II)-loaded polymeric micelles directed to improved tumour targeting and enhanced antitumour activity. *J. Control. Release* **121,** 146–155 (2007).
11. Maruyama, K., Ishida, O., Takizawa, T. & Moribe, K. Possibility of active targeting to tumor tissue with liposome. *Adv. Drug Deliv. Rev.* **40,** 89–102 (1999).
12. Lammers, T. *et al.* Image-guided and passively tumor-targeted polymeric nanomedicines for radiochemotherapy. *Br. J. Cancer* **99,** 900–910 (2008).
13. Matsumura, Y. & Kataoka, K. Preclinical and clinical studies of anticancer agent-incorporating polymer micelles. *Cancer Sci.* **100,** 572–579 (2009).
14. Matsumura, Y. Preclinical and clinical studies of NK012, an SN-38-incorporating polymeric micelles, which is designed based on EPR effect. *Adv. Drug Deliv. Rev.* **63,** 184–192 (2011).

15. Working, P. K. *et al.* Pharmacokinetics, biodistribution and therapeutic efficacy of doxorubicin encapsulated in stealth liposomes (DOXIL). *J. Liposome Res.* **4,** 667–687 (1994).
16. Northfelt, D. W. *et al.* Pegylated-liposomal doxorubicin versus doxorubicin, bleomycin, and vincristine in the treatment of AIDS-related Kaposi's sarcoma: results of a randomized phase III clinical trial. *J. Clin. Oncol.* **16,** 2445–2451 (1998).
17. Gradishar, W. J. *et al.* Phase III trial of nanoparticle albumin-bound paclitaxel compared with polyethylated castor oil-based paclitaxel in women with breast cancer. *J. Clin. Oncol.* **23,** 7794–7803 (2005).
18. Uster, P. S., Working, P. K. & Vaage, J. Pegylated liposomal doxorubicin (DOXIL(R), CAELYX(R)) distribution in tumour models observed with confocal laser scanning microscopy. *Int. J. Pharm.* **162,** 77–86 (1998).
19. Unezaki, S. *et al.* Direct measurement of the extravasation of polyethyleneglycol-coated liposomes into solid tumor tissue by *in vivo* fluorescence microscopy. *Int. J. Pharm.* **144,** 11–17 (1996).
20. Kano, M. R. *et al.* Improvement of cancer-targeting therapy, using nanocarriers for intractable solid tumours by inhibition of TGF-β signaling. *Proc. Natl Acad. Sci. USA* **104,** 3460–3465 (2007).
21. Dreher, M. *et al.* Tumour vascular permeability, accumulation, and penetration of macromolecular drug carriers. *J. Natl Cancer Inst.* **98,** 330–343 (2006).
22. Perrault, S. D., Walkey, C., Jennings, T., Fischer, H. C. & Chan, W. C. W. Mediating tumour targeting efficiency of nanoparticles through design. *Nano Lett.* **9,** 1909–1915 (2009).
23. Aliabadi, H. M. & Lavasanifar, A. Polymeric micelles for drug delivery. *Exp. Opin. Drug. Deliv.* **3,** 139–162 (2006).
24. Matsumura, Y. *et al.* Phase I clinical trial and pharmacokinetic evaluation of NK911, a micelle-encapsulated doxorubicin. *Br. J. Cancer* **91,** 1775–1781 (2004).
25. Plummer, R. *et al.* A phase I clinical study of cisplatin-incorporated polymeric micelles (NC-6004) in patients with solid tumours. *Br. J. Cancer* **104,** 593–598 (2011).
26. Cabral, H., Nishiyama, N., Okazaki, S., Kato, Y. & Kataoka, K. Preparation and biological properties of dichloro(1,2-diaminocyclohexane)platinum(II) (DACHPt)-loaded polymeric micelles. *J. Control. Release* **101,** 223–232 (2005).
27. Nishiyama, N. & Kataoka, K. Preparation and characterization of size-controlled polymeric micelle containing *cis*-dichlorodiammineplatinum(II) in the core. *J. Control. Release* **74,** 83–94 (2001).
28. Murakami, M. *et al.* Improving drug potency and efficacy by nanocarrier-mediated subcellular targeting. *Sci. Transl. Med.* **3,** 64ra2 (2011).
29. Alexis, F., Pridgen, E., Molnar, L. K. & Farokhzad, O. C. Factors affecting the clearance and biodistribution of polymeric nanoparticles. *Mol. Pharm.* **5,** 505–515 (2008).
30. Verma, A. *et al.* Surface-structure-regulated cell-membrane penetration by monolayer-protected nanoparticles. *Nature Mater.* **7,** 588–595 (2008).
31. Kano, M. R. *et al.* Comparison of the effects of the kinase inhibitors imatinib, sorafenib, and transforming growth factor-β receptor inhibitor on extravasation of nanoparticles from neovasculature. *Cancer Sci.* **100,** 173–180 (2009).
32. Takahashi, Y. *et al.* Significance of vessel count, vascular endothelial growth factor, and its receptor (KDR) in intestinal-type gastric cancer. *Clin. Cancer Res.* **2,** 1679–1684 (1996).
33. Sofuni, A. *et al.* Differential diagnosis of pancreatic tumours using ultrasound contrast imaging. *J. Gastroenterol.* **40,** 518–525 (2005).
34. Matsumoto, Y. *et al.* Direct and instantaneous observation of intravenously injected substances using intravital confocal micro-videography. *Biomed. Optics Exp.* **1,** 1209–1216 (2010).
35. Choi, H. S. *et al.* Renal clearance of quantum dots. *Nature Biotechnol.* **25,** 1165–1170 (2007).
36. Terada, Y. *et al.* Construction and commissioning of BL37XU at SPring-8. *AIP Conf. Proc.* **705,** 376–379 (2004).

Acknowledgements

The authors are grateful to S. Fukuda from the University of Tokyo Hospital for his valuable support in conducting transmission electron microscopy and to S. Ogura for assistance with animal care. This study was supported by the Funding Program for World-Leading Innovative R&D on Science and Technology (FIRST Program) from the Japan Society for the Promotion of Science (JSPS) and Grants-in-Aid for Scientific Research from the Japanese Ministry of Health, Labour, and Welfare. μ-SR-XRF studies were supported by the Nanotechnology Support Program of the Japan Synchrotron Radiation Research Institute (JASRI).

Author contributions

H.C. designed and performed all the experiments. Y.M. assisted with *in vivo* confocal microscopies. K.M. and Y.T. helped in the μ-X-ray fluorescence measurements. Q.C. performed transmission electron microscopy of the micelles. M.M and M.K. aided in the biodistribution experiments. H.C. wrote the manuscript. M.R.K., K.M. and M.U. commented on the manuscript. N.N. and K.K. edited the manuscript. K.K., with help from N.N., supervised the whole project.

Additional information

The authors declare no competing financial interests. Supplementary information accompanies this paper at www.nature.com/naturenanotechnology. Reprints and permission information is available online at http://www.nature.com/reprints. Correspondence and requests for materials should be addressed to N.N. and K.K.

Journal of Controlled Release 151 (2011) 104–109

Contents lists available at ScienceDirect

Journal of Controlled Release

journal homepage: www.elsevier.com/locate/jconrel

Concept Paper

In situ quantitative monitoring of polyplexes and polyplex micelles in the blood circulation using intravital real-time confocal laser scanning microscopy

Takahiro Nomoto [a,1], Yu Matsumoto [b,c,d,1], Kanjiro Miyata [b], Makoto Oba [e], Shigeto Fukushima [f], Nobuhiro Nishiyama [b], Tatsuya Yamasoba [c], Kazunori Kataoka [a,b,f,*]

[a] Department of Bioengineering, Graduate School of Engineering, The University of Tokyo, Japan
[b] Division of Clinical Biotechnology, Center for Disease Biology and Integrative Medicine, Graduate School of Medicine, The University of Tokyo, Japan
[c] Department of Otorhinolaryngology and Head and Neck Surgery, Graduate School of Medicine and Faculty of Medicine, The University of Tokyo, Japan
[d] Department of Otorhinolaryngology and Head and Neck Surgery, Mitsui Memorial Hospital, Japan
[e] Department of Vascular Regeneration, Division of Tissue Engineering, The University of Tokyo Hospital, Japan
[f] Department of Materials Engineering, Graduate School of Engineering, The University of Tokyo, Japan

ARTICLE INFO

Article history:
Received 12 January 2011
Accepted 10 February 2011
Available online 3 March 2011

Keywords:
Intravital confocal microscopy
Polyplex
Polyethylene glycol
Block copolymer
Polymer micelle

ABSTRACT

Surface modification using poly(ethylene glycol) (PEG) is a widely used strategy to improve the biocompatibility of cationic polymer-based nonviral gene vectors (polyplexes). A novel method based on intravital real-time confocal laser scanning microscopy (IVRTCLSM) was applied to quantify the dynamic states of polyplexes in the bloodstream, thereby demonstrating the efficacy of PEGylation to prevent their agglomeration. Blood flow in the earlobe blood vessels of experimental animals was monitored in a noninvasive manner to directly observe polyplexes in the circulation. Polyplexes formed distinct aggregates immediately after intravenous injection, followed by interaction with platelets. To quantify aggregate formation and platelet interaction, the coefficient of variation and Pearson's correlation coefficient were adopted. In contrast, polyplex micelles prepared through self-assembly of plasmid DNA with PEG-based block catiomers had dense PEG palisades, revealing no formation of aggregates without visible interaction with platelets during circulation. This is the first report of *in situ* monitoring and quantification of the availability of PEGylation to prevent polyplexes from agglomeration over time in the blood circulation. This shows the high utility of IVRTCLSM in drug and gene delivery research.

1. Concept of new methodologies

Gene therapy offers a unique potential for the treatment of genetic and intractable diseases and for tissue engineering. Its success is dependent upon the development of useful gene vectors as well as application of a drug delivery system (DDS). Nonviral gene vectors are attractive alternatives to viral gene vectors because they are much simpler to produce, transport and store, and induce fewer immune responses. Cationic polymers that electrostatically interact with plasmid DNA (pDNA) have been widely studied as materials to construct nonviral gene vectors [1–5]. The cationic polymers most commonly used as gene vectors include branched polyethylenimine (BPEI), linear polyethylenimine, poly(L-lysine) (PLys), chitosan, and dendrimers [6]. These polymers form polyion complexes (polyplexes) with pDNA to successfully transfer it into cultured cells to induce appreciable level of gene expression. However, these polyplexes have biocompatibility problems for systemic application. Polyplexes usually require excess polycations to generate electrostatic repulsion for their increased solubility and colloidal stability. This eventually results in a shift of their surface charge to a positive value. This positive charge causes nonspecific interaction with anionic components in the body such as plasma proteins and blood cells, which might lead to severe adverse effects [7,8]. Attachment of hydrophilic polymers such as poly(ethylene glycol) (PEG) is called "PEGylation" and has often been used to shield nonviral gene vectors from undesired interaction in the blood. PEGylation also contributes to diminished uptake by the reticuloendothelial system or macrophages, and hence the half-life in blood circulation can be extended.

It is well documented that a PEG palisade prevents nonspecific interaction with biological components. However, *in situ* evaluation of

Abbreviations: PEG, poly(ethylene glycol); DDS, drug delivery system; pDNA, plasmid DNA; BPEI, branched polyethylenimine; PLys, poly(L-lysine); PEG-PLys, poly(ethylene glycol)-*b*-poly(L-lysine); PAsp(DET), poly{*N*-[*N*-(2-aminoethyl)-2-aminoethyl]aspartamide}; PEG-PAsp(DET), poly(ethylene glycol)-*b*-poly{*N*-[*N*-(2-aminoethyl)-2-aminoethyl] aspartamide}; IVRTCLSM, intravital real-time confocal laser scanning microscopy; CV, coefficient of variation; PCC, Pearson's correlation coefficient.

* Corresponding author at: Department of Materials Engineering, Graduate School of Engineering, The University of Tokyo, 7-3-1 Hongo, Bunkyo-ku, Tokyo 113-0033, Japan. Tel.: +81 3 5841 7138; fax: +81 3 5841 7139.
E-mail address: kataoka@bmw.t.u-tokyo.ac.jp (K. Kataoka).

[1] These authors equally contributed to this work.

0168-3659/$ – see front matter © 2011 Elsevier B.V. All rights reserved.
doi:10.1016/j.jconrel.2011.02.011

the interaction between nonviral gene vectors and biological components has not been reported due to the absence of methodology to quantify the interaction. We recently described a method of direct and instantaneous observation of intravenously injected substances using intravital real-time confocal laser scanning microscopy (IVRTCLSM) [9]. IVRTCLSM provides high-speed scanning and simultaneous capture of multicolor fluorescence. The macromolecular agents flowing in the bloodstream in tumors, kidneys, and livers can be monitored using IVRTCLSM.

In the present study, we applied IVRTCLSM for the investigation of the interaction between nonviral gene vectors and biological components *in situ*. For the PEGylated polyplexes, we focused on polyplex micelles made through the self-assembly of pDNA with PEG-based cationic block copolymers [10–12]. We further developed an analytical methodology to quantify the dynamic states of nonviral gene vectors circulating in the bloodstream. This is the first report visualizing and quantifying the interaction between nonviral gene vectors and biological components over time and in real-time *in situ*.

2. Experimental methods

2.1. Sample preparation

Sterile Hepes (1 M, pH 7.3) was purchased from Amresco (Solon, OH, USA) and used as a buffer solution after dilution with distilled water. pDNA encoding the soluble form of vascular endothelial growth factor receptor-1 was labeled with Cy5 using Label IT Tracker Nucleic Acid Localization Kits (Mirus Bio Corporation, Madison, WI, USA). BPEI (molecular weight (MW) 22 kDa; Sigma-Aldrich, St. Louis, MO, USA) was dialyzed in 0.01 M HCl and lyophilized as a hydrochloride salt. BPEI and PLys (hydrobromide salt, MW 4–15 kDa; Sigma-Aldrich) were mixed with Cy5-labeled pDNA (150 μg/mL) at an N/P ratio of 6 and 2, respectively, to form polyplexes. The N/P ratio was defined as the residual molar ratio of amino groups of cationic segment to phosphate groups of pDNA. Poly{*N*-[*N*-(2-aminoethyl)-2-aminoethyl]aspartamide} (PAsp(DET)) (polymerization degree: 95) was synthesized as described previously [13]. PAsp(DET) was mixed with Cy5-labeled pDNA at an N/P ratio of 4. Poly(ethylene glycol)-*b*-poly(L-lysine) (PEG-PLys; MW of PEG: 12,000; polymerization degree of PLys segment: 45) was synthesized as described previously [14]. Poly(ethylene glycol)-*b*-poly{*N*-[*N*-(2-aminoethyl)-2-aminoethyl]aspartamide} (PEG-PAsp(DET); MW of PEG: 12,000 Da; polymerization degree of PAsp(DET) segment: 93) was synthesized by the aminolysis of PEG-poly(β-benzyl L-aspartate) block copolymer with diethylenetriamine according to a previous report [13]. PEG-PLys/pDNA and PEG-PAsp(DET)/pDNA micelles were prepared at an N/P ratio of 2 and 4, respectively. The final Cy5-labeled pDNA concentration was adjusted to 100 μg/mL in 10 mM Hepes buffer (pH 7.3).

2.2. Animal preparation

All animal experimental procedures were executed in accordance with the Guide for the Care and Use of Laboratory Animals as stated by the National Institutes of Health. Balb/c nude mice (female; Charles River Laboratories, Tokyo, Japan) were anesthetized with 3.0%–4.0% isoflurane (Abbott Japan Co., Ltd., Tokyo, Japan) using a Univenter 400 Anaesthesia Unit (Univentor Ltd., Zejtun, Malta). Mice were then subjected to lateral tail vein catheterization with a 30-gauge needle (Dentronics Co., Ltd., Tokyo, Japan) connected to a nontoxic, medical grade polyethylene tube (Natsume Seisakusho Co., Ltd., Tokyo, Japan). Platelets were labeled *in vivo* with the intravenous injection of DyLight 488-conjugated anti-GPIbβ antibody (X488; EMFRET Analytics, Eibelstadt, Germany) following the manufacturer's instructions. Mice were placed onto a custom-designed temperature-controlled microscope stage. The ear lobe was attached beneath the cover slip with a single drop of immersion oil as described in our previous report [9]. Video acquisition of the dermis tissue at a speed of 30 frames per second was performed for 10 min. Two-hundred microliters of naked pDNA, polyplexes, and micelles (20 μg of pDNA) were administered via the tail vein catheter 10 s after video acquisition was initiated. For the platelet inhibition study, 300 μL of aspirin (acetylsalicylic acid; Sigma-Aldrich) saturated aqueous solution was orally administered to mice for 2 consecutive days before IVRTCLSM.

2.3. IVRTCLSM imaging and processing

All picture/movie acquisitions were performed using a Nikon A1R confocal laser scanning microscope system attached to an upright ECLIPSE FN1 machine equipped with a CFI Apo 40× WI λS objective lens (Nikon, Tokyo, Japan). All pictures/movies were acquired at a scale of 79.55 μm × 79.55 μm with 5.11 μm of confocal slice. Acquired data were further processed using Nikon NIS Elements software. The region of interest (ROI) was manually defined in the vein. Image frames were extracted every 5 s from the video data for further analyses. For quantification of aggregates, the coefficient of variation (CV) of Cy5 fluorescence was calculated. For the platelet interaction study, colocalization between DyLight and Cy5 was evaluated by Pearson's correlation coefficient (PCC) [15]. All obtained values were plotted against time.

3. Discovery

3.1. Real-time observation of aggregates

We prepared BPEI/pDNA (N/P = 6), PLys/pDNA (N/P = 2), and PAsp (DET)/pDNA (N/P = 4) polyplexes as well as PEG-PLys/pDNA (N/P = 2) and PEG-PAsp(DET)/pDNA (N/P = 4) micelles. BPEI/pDNA was used as the representative polyplex containing excessive polycations. N/P ratios of PLys/pDNA and PAsp(DET)/pDNA were determined as the critical ratio to condense pDNA according to our previous report [16]. N/P ratios of PEG-PLys/pDNA and PEG-PAsp(DET)/pDNA micelles were determined at the same N/P ratios of PLys/pDNA and PAsp(DET)/pDNA polyplexes, respectively. The size and zeta potentials of these polyplexes and polyplex micelles were summarized in Supplementary Table 1.

Intravenously injected polyplexes and micelles were directly observed by IVRTCLSM. These dynamic states in the bloodstream were compared (Supplementary Videos 1–5). Extracted movie frames at indicated time points are shown in Fig. 1. Immediately after the BPEI/pDNA polyplex was injected, the fluorescence of Cy5 agglomerated into clumps with a variable size in several micrometers range. This nonuniform fluorescence distribution of the polyplex indicated formation of aggregates. PLys/pDNA and PAsp(DET)/pDNA polyplexes showed similar aggregate formation. In contrast, the fluorescence of Cy5 showed uniform distribution when PEG-PLys/pDNA and PEG-PAsp(DET)/pDNA micelles were injected, indicating the absence of aggregates.

3.2. Quantification of aggregates

Using the mean intensity of Cy5 fluorescence, the amount of Cy5-labeled pDNA was evaluated. We acquired the images every 5 s, calculated the relative fluorescence intensity defined as (Cy5 mean fluorescence intensity - Cy5 minimum fluorescence intensity)/(Cy5 maximum fluorescence intensity − Cy5 minimum fluorescence intensity), and plotted the relative fluorescence intensities against time. (Supplementary Fig. 1) The relative fluorescence intensities of naked pDNA decreased immediately, and almost disappeared within 5 min after the start of acquisition. The relative fluorescence intensities of BPEI/pDNA, PLys/pDNA, and PAsp(DET)/pDNA polyplexes also rapidly decreased and dropped to around 0.2 within 10 min after the start of acquisition. In contrast, PEG-PLys/pDNA, and PEG-PAsp(DET)/pDNA polyplex micelles maintained the relative

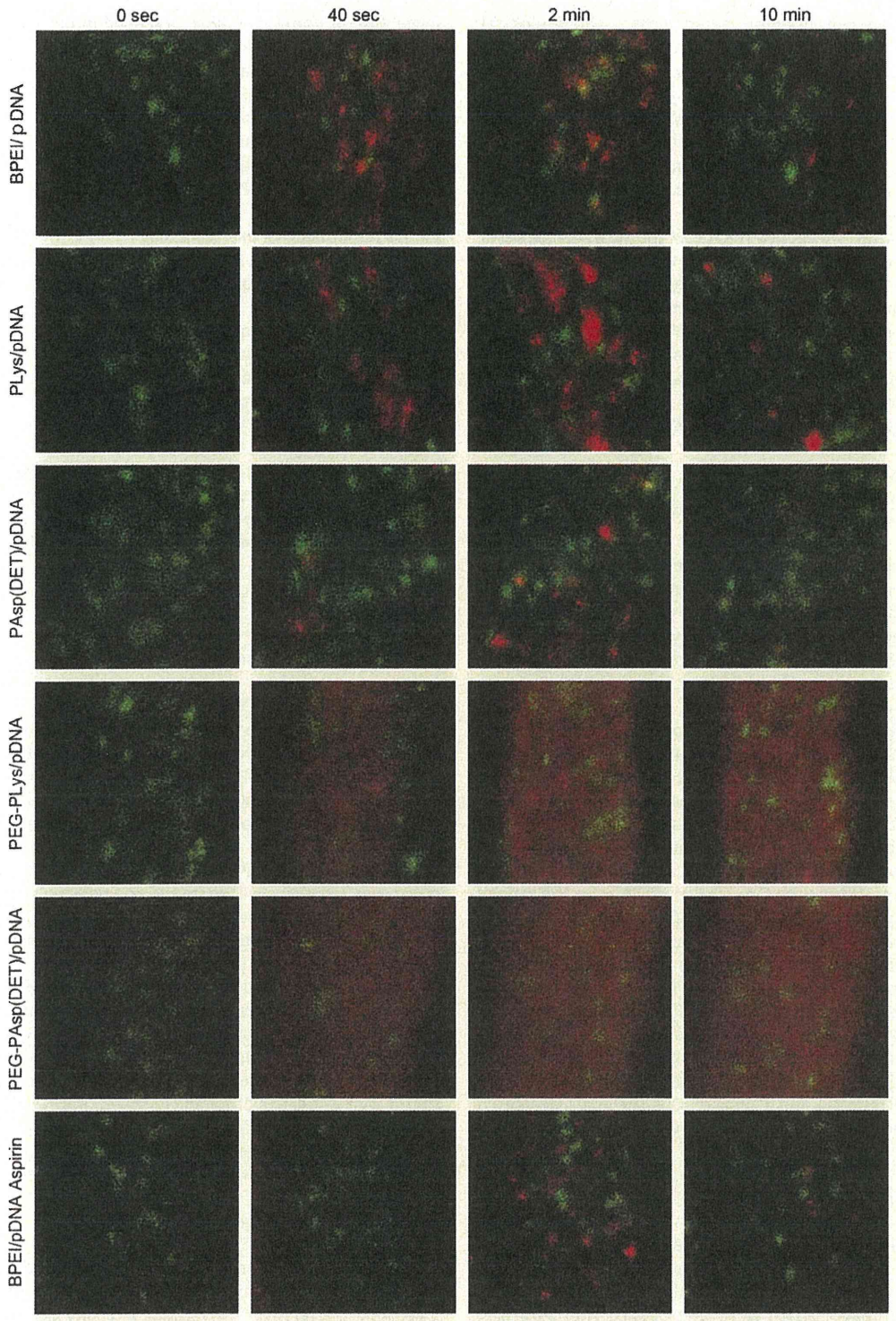

Fig. 1. Intravital confocal micro-videography of polyplexes and polyplex micelles in the bloodstream of the mouse earlobe. Prior to observation, the anti-GPIbβ antibody conjugated with DyLight 488 was injected to label platelets (green). The polyplexes and polyplex micelles incorporating Cy5-labeled pDNA (red) were intravenously injected 10 s after start of observation. Image frames were extracted from videos at identical time points for comparison. Image size: 79.55 μm × 79.55 μm. Confocal slice: 5.11 μm.

fluorescence intensities of around 0.9 and 0.7 even 10 min after the start of acquisition, suggesting the prolonged blood circulation. These results are consistent with the previous studies, which demonstrated pDNA degradation within 5 min and the improvement of blood circulation by PEGylation [17,18].

However, the relative fluorescence intensities could not provide the information about the aggregates of polyplexes and polyplex micelles. Thus, the quantification of aggregates was performed by CV calculation of Cy5 fluorescence in the ROI. The CV is a normalized measure of dispersion of a distribution, and is defined as the ratio of

the standard deviation to the mean. We acquired the images every 5 s, calculated the CV, and plotted the CV against time (Fig. 2). CV values of the polyplexes rapidly increased upon first entry into the vein of the earlobe immediately after intravenous injection. CV values of the polyplexes subsequently fluctuated and decreased over time. In contrast, CV values of the micelles slightly increased upon first entry due to the admixture of micelles and blood, and remained at a plateau at the lower values without fluctuation.

3.3. Platelet interaction study

Platelet is known to be the primary cell components involved in the initial event of thrombosis, and polycations initiate the process of platelet clots formation [19–21]. Thus, in this study, we focused on platelets interaction with cationic polyplexes. To investigate the interaction of polyplexes with platelets, we labeled platelets with DyLight 488-conjugated anti-GPIbβ antibody, and observed the interaction using IVRTCLSM (Fig. 1, Supplementary Videos 1–5). The average labeling efficiency of the antibody has been reported to be ~90% [22]. BPEI/pDNA, PLys/pDNA, and PAsp(DET)/pDNA polyplexes formed aggregates immediately after injection as described above. Their adhesion to platelets was clearly observed approximately 2 min after injection as judged from the colocalization of red and green fluorescences to appear as yellow colored pixels. In contrast, PEG-PLys/pDNA and PEG-PAsp(DET)/pDNA micelles showed no adhesion to platelets throughout the whole experiment.

3.4. Platelet interaction quantification

To quantify the interaction between polyplexes and platelets, we acquired the images every 5 s, and calculated the colocalization between Cy5 fluorescence and DyLight 488 fluorescence using PCC [15]. PCC indicates the intensity of the correlation of two elements, ranging from −1 to +1. The PCC value of the BPEI/pDNA polyplex fluctuated and increased up to approximately 0.4 (Fig. 3). PLys/pDNA and PAsp(DET)/pDNA polyplexes also fluctuated and increased up to approximately 0.25 and 0.33, respectively. In contrast, PCC values of PEG-PLys/pDNA and PEG-PAsp(DET)/pDNA micelles were maintained at almost zero throughout the study.

3.5. Platelet inhibition study

To investigate whether inhibition of platelet function decreases aggregates formation, aspirin was used as an anti-platelet agent. We compared the CV and PCC of the BPEI/pDNA polyplex between aspirin-administered mice and nonadministered control mice (Figs. 1 and 4, Supplementary Video 6). The CV value of the aspirin-administered mice was almost identical to that of control mice; however, their PCC value remained <0.1 throughout the study.

4. Interpretation and significance of new methodologies

Pharmacokinetic studies are indispensable for developing efficient DDSs that transport drugs specifically to the targeted tissue. Pharmacokinetic studies using animals have primarily relied on *ex vivo* techniques, such as analyzing blood or urine samples. These *ex vivo* techniques have been well established to analyze blood circulation, target accumulation, or other pharmacological information of the DDS. However, this approach provides only static information at specific time points. Therefore, investigating dynamic and longitudinal events using this approach is difficult. Alternatively, the intravital microscopy is an emerging technique [23], allowing to investigate such dynamic states of DDS in animals. Recently, we developed the intravital microscopy equipped with fast-scanning laser confocal systems (IVRTCLSM) [9], and demonstrated here its application as a novel tool to dynamically evaluate the interaction between gene vectors and blood components. Our method is characterized by noninvasive observation with high spatial and temporal resolutions to quantitatively monitor the dynamic states

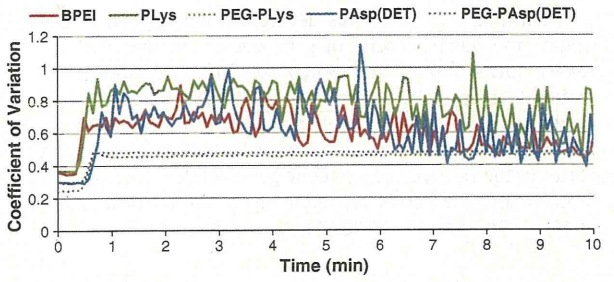

Fig. 2. Quantification of aggregates of polyplexes and micelles. Aggregates of polyplexes and micelles were quantified with CV of Cy5 fluorescence intensities in the frames extracted every 5 s from crude videos.

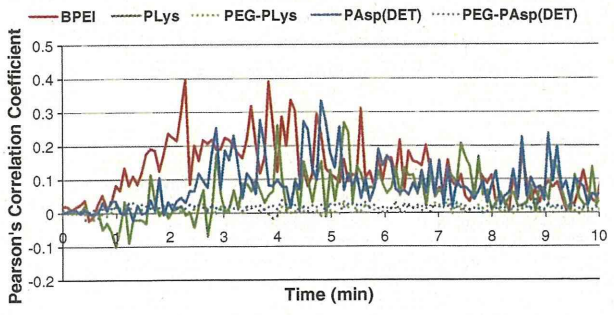

Fig. 3. Quantification of colocalization between polyplexes/micelles and platelets. The colocalization was measured with PCC. PCC was calculated from the frames extracted every 5 s from crude videos.

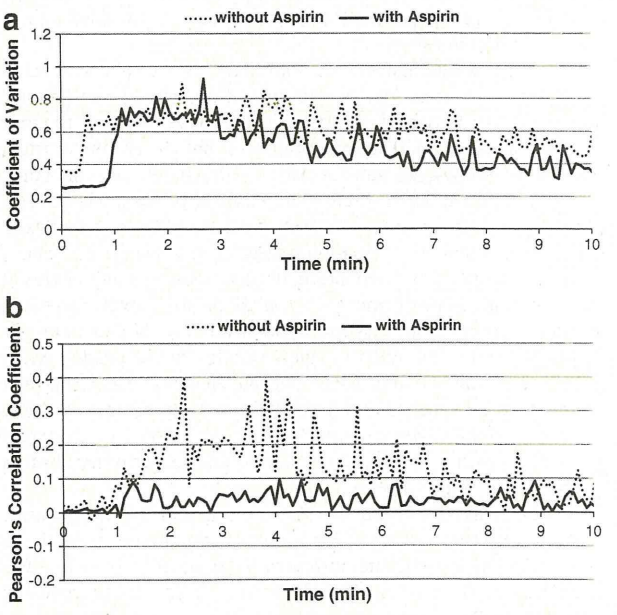

Fig. 4. Platelets inhibition study with aspirin. (a) Aggregates of BPEI/pDNA polyplexes of the aspirin-administered mouse was quantified with the CV of Cy5 fluorescence intensities in the frames extracted every 5 s from crude videos. (b) Colocalization between BPEI/pDNA polyplexes and platelets of the aspirin-administered mouse was quantified with PCC. PCC was calculated from the frames extracted every 5 s from crude videos. For comparison, the CV and PCC of the BPEI/pDNA polyplexes-administered normal mouse in Figs. 2 and 3 were shown respectively again.

of nonviral gene vectors. In the present study, the mouse earlobe was noninvasively fixed beneath the coverslip, and the vein was imaged at the dermis layer. Confocal imaging eliminated light from out-of-focus sections in the ear lobe such as the epidermis and hypodermis. Furthermore, we kept the confocal slice thinner (5.11 μm) than the diameter of the vein, so that the signal was detected only from inside the vasculature. High-speed scanning was essential to obtain unambiguous images to quantify the aggregates and colocalization between nonviral gene vectors and platelets because conventional galvano scanners are too slow to distinguish the individual aggregates and platelets rapidly flowing in the bloodstream, providing insufficient and blurred images (Supplementary Videos 7 and 8).

We investigated the polycations BPEI and PLys. They are widely used to construct polyplexes and PAsp(DET) has reduced cytotoxicity and high transfection efficiency [13]. To evaluate the improvement of biocompatibility via PEGylation, PEG-PLys/pDNA and PEG-PAsp (DET)/pDNA micelles were examined. A simple and effective way to PEGylate polyplexes is, as we reported [10–12], to use PEG-based cationic block copolymers as counterpart polycations to pDNA. The block copolymers are characterized by tandem alignment of a hydrophilic PEG segment and a cationic segment, leading to the formation of stable and biocompatible micelles with a core of polycation/pDNA complex surrounded by a dense PEG palisade and size of approximately 100 nm. Indeed, the micelle composed of PEG-PLys and pDNA achieved higher stability than that of unmodified PLys/pDNA polyplex in a medium containing serum and showed prolonged blood circulation [18,24]. The block copolymer possessing a cationic polyaspartamide segment carrying an ethylenediamine unit at the side chain, PEG-PAsp(DET), also formed the micelle with pDNA, which prevented nonspecific interaction with biological components such as erythrocytes and platelets under *in vitro* conditions [8].

IVRTCLSM was used to directly investigate the interaction between these gene vectors and platelets in the bloodstream. IVRTCLSM could be used to evaluate the dynamic states of nonviral gene vectors rapidly flowing in the bloodstream over time *in situ* (Fig. 1 and Supplementary Videos 1–6). This is the first report to visualize the formation of aggregates and the prevention by PEGlyation of polyplexes *in situ* in the bloodstream.

To quantify the aggregates, we adopted the CV. CV values reflected the nonuniform fluorescence distribution of polyplexes and uniform fluorescence distribution of micelles (Fig. 2). It is noteworthy that our IVRTCLSM started video acquisition 10 s before administration, allowing us to follow aggregate formation immediately after injection. CV values of the polyplexes rapidly increased approximately 20–30 s after injection, and corresponded well with the entry of polyplexes, indicating instantaneous formation of aggregates (Fig. 2). CV values also fluctuated over time, depending on the amount of aggregates at those time points. Furthermore, CV values of polyplexes decreased with time due to their disappearance from the bloodstream. In contrast, CV values of micelles were moderately elevated when micelles passed the ROI first. This moderate elevation was because of the admixture of micelles and blood without aggregate formation. Moreover, CV values were retained at a plateau after this moderate elevation, suggesting persistent circulation and uniform distribution of micelles in the bloodstream.

IVRTCLSM was also useful for the investigation of the dynamic interaction between nonviral gene vectors and platelets. Indeed, we succeeded in visualizing the interaction between polyplexes and platelets *in situ*. This dynamic information could not be revealed without IVRTCLSM.

To quantify the platelet interaction, we adopted PCC between polyplexes/micelles and platelets (Fig. 3). PCC values of polyplexes did not increase at the time point when CV values started to increase. PCC values began to increase after approximately 1 min after injection, and indicated strong correlation between polyplexes and platelets 2 min after injection. This temporal gap between aggregate formation and platelet interaction strongly indicated that aggregate formation was not triggered by platelets. To confirm this, we conducted the study in mice that were administered aspirin (Fig. 4). Aspirin induces a long-lasting functional defect in platelets [25], and thus may inhibit platelet interaction with polyplexes. The CV and PCC quantitatively demonstrated that oral administration of aspirin successfully inhibited platelet interaction with aggregates (Fig. 4b), but did not inhibit aggregate formation itself (Fig. 4a). This result indicates that the aggregate formation of polyplexes does not involve platelets (at least in the initial stage). Presumably, some protein components in plasma may have a role in aggregate formation, but further investigation is needed to clarify the mechanism.

Aggregate formation in the range of several micrometers immediately after intravenous injection should crucially affect the efficiency of systemically injected polyplexes. The aggregated polyplexes cannot extravasate into the targeted tissues or cells. Moreover, they might lead to thrombosis through the interaction with platelets to obstruct microvessels in normal tissue, including the lungs and liver, resulting in nonspecific accumulation of polyplexes in these tissues. This accumulation caused by aggregate formation will lead to unfavorable effects such as pulmonary embolism. The micelles, in contrast, did not form aggregates, and also showed no interaction with platelets. Thus, they are expected to prevent adverse effects caused by polyplex agglomeration, which cannot be inhibited even by oral administration of aspirin. This result confirms that PEGylation is a rational strategy to improve the biocompatibility of nonviral gene vectors based on polyplex formation [3,10–12].

In the present study, IVRTCLSM was used to visualize and quantify the dynamic states of polyplexes flowing in the bloodstream. Moreover, with respect to ethics, IVRTCLSM excels conventional *ex vivo* methods that involve the sacrifices of numerous animals to acquire pharmacokinetic information. IVRTCLSM provides temporal and spatial information at 30 time points in 1 s with a single mouse, which is desirable for high-throughput screening of newly developed DDSs.

In conclusion, IVRTCLSM was developed and applied to directly investigate the dynamic state of gene vectors in the bloodstream. Aggregate formation of the polyplexes and its prevention by PEGylation was observed *in situ* for the first time under the flow in the capillary. Thus, IVRTCLSM could provide the requisite information that has not been obtained by conventional methods, thereby giving a new facet in the research on systemic gene delivery.

Supplementary materials related to this article can be found online at doi:10.1016/j.jconrel.2011.02.011.

Acknowledgment

This work was supported in part by Core Research Program for Evolutional Science and Technology (CREST) from the Japan Science and Technology Corporation (JST) and Funding Program for World-Leading Innovative R&D on Science and Technology (FIRST Program) from Japan Society for the Promotion of Science (JSPS).

References

[1] D.W. Pack, A.S. Hoffman, S. Pun, P.S. Stayton, Design and development of polymers for gene delivery, Nat. Rev. Drug Discov. 4 (2005) 581–593.
[2] T. Merdan, K. Kunath, H. Petersen, U. Bakowsky, K.H. Voigt, J. Kopecek, T. Kissel, PEGylation of poly(ethylene imine) affects stability of complexes with plasmid DNA under in vivo conditions in a dose-dependent manner after intravenous injection into mice, Bioconjug. Chem. 16 (2005) 785–792.
[3] M. Ogris, E. Wagner, Targeting tumors with non-viral gene delivery systems, Drug Discov. Today 7 (2002) 479–485.
[4] Y. Kakizawa, K. Kataoka, Block copolymer micelles for delivery of gene and related compounds, Adv Drug Deliver Rev 54 (2002) 203–222.

[5] K. Osada, R.J. Christie, K. Kataoka, Polymeric micelles from poly(ethylene glycol)-poly(amino acid) block copolymer for drug and gene delivery, J. R. Soc. Interface 6 (2009) S325–S339.
[6] Y.Y. Yang, Y. Wang, R. Powell, P. Chan, Polymeric core–shell nanoparticles for therapeutics, Clin. Exp. Pharmacol. Physiol. 33 (2006) 557–562.
[7] M. Ogris, S. Brunner, S. Schuller, R. Kircheis, E. Wagner, PEGylated DNA/transferrin-PEI complexes: reduced interaction with blood components, extended circulation in blood and potential for systemic gene delivery, Gene Ther. 6 (1999) 595–605.
[8] D. Akagi, M. Oba, H. Koyama, N. Nishiyama, S. Fukushima, T. Miyata, H. Nagawa, K. Kataoka, Biocompatible micellar nanovectors achieve efficient gene transfer to vascular lesions without cytotoxicity and thrombus formation, Gene Ther. 14 (2007) 1029–1038.
[9] Y. Matsumoto, T. Nomoto, H. Cabral, Y. Matsumoto, S. Watanabe, R.J. Christie, K. Miyata, M. Oba, T. Ogura, Y. Yamasaki, N. Nishiyama, T. Yamasoba, K. Kataoka, Direct and instantaneous observation of intravenously injected substances using intravital confocal micro-videography, Biomed. Opt. Express 1 (2010) 1209–1216.
[10] K. Osada, R.J. Christie, K. Kataoka, Polymeric micelles from poly(ethylene glycol)-poly(amino acid) block copolymer for drug and gene delivery, J. R. Soc. Interface 6 (Suppl. 3) (2009) S325–339.
[11] Y. Kakizawa, K. Kataoka, Block copolymer micelles for delivery of gene and related compounds, Adv. Drug Deliv. Rev. 54 (2002) 203–222.
[12] N. Nishiyama, K. Kataoka, Current state, achievements, and future prospects of polymeric micelles as nanocarriers for drug and gene delivery, Pharmacol. Ther. 112 (2006) 630–648.
[13] K. Itaka, T. Ishii, Y. Hasegawa, K. Kataoka, Biodegradable polyamino acid-based polycations as safe and effective gene carrier minimizing cumulative toxicity, Biomaterials 31 (2010) 3707–3714.
[14] A. Harada, K. Kataoka, Formation of polyion complex micelles in an aqueous milieu from a pair of oppositely-charged block-copolymers with poly(ethylene glycol) segments, Macromolecules 28 (1995) 5294–5299.
[15] V. Zinchuk, O. Zinchuk, T. Okada, Quantitative colocalization analysis of multicolor confocal immunofluorescence microscopy images: pushing pixels to explore biological phenomena, Acta Histochem. Et Cytochem. 40 (2007) 101–111.
[16] K. Miyata, S. Fukushima, N. Nishiyama, Y. Yamasaki, K. Kataoka, PEG-based block catiomers possessing DNA anchoring and endosomal escaping functions to form polyplex micelles with improved stability and high transfection efficacy, J. Control. Release 122 (2007) 252–260.
[17] K. Kawabata, Y. Takakura, M. Hashida, The fate of plasmid dna after intravenous-injection in mice — involvement of scavenger receptors in its hepatic-uptake, Pharm. Res. 12 (1995) 825–830.
[18] M. Harada-Shiba, K. Yamauchi, A. Harada, I. Takamisawa, K. Shimokado, K. Kataoka, Polyion complex micelles as vectors in gene therapy — pharmacokinetics and in vivo gene transfer, Gene Ther. 9 (2002) 407–414.
[19] K. Kataoka, T. Tsuruta, T. Akaike, Y. Sakurai, Biomedical behavior of synthetic polyion complexes toward blood-platelets, Makromolekulare Chem. Macromol. Chem. Phys. 181 (1980) 1363–1373.
[20] T.K. Rosborough, Parallel inhibition of ristocetin and polycation-induced platelet agglutination, Thromb. Res. 19 (1980) 417–422.
[21] P. Chollet, M.C. Favrot, A. Hurbin, J.L. Coll, Side-effects of a systemic injection of linear polyethylenimine–DNA complexes, J. Gene Med. 4 (2002) 84–91.
[22] M.R. Dowling, E.C. Josefsson, K.J. Henley, P.D. Hodgkin, B.T. Kile, Platelet senescence is regulated by an internal timer, not damage inflicted by hits, Blood 116 (2010) 1776–1778.
[23] S. Hak, N.K. Reitan, O. Haraldseth, C. Lange Davies, Intravital microscopy in window chambers: a unique tool to study tumor angiogenesis and delivery of nanoparticles, Angiogenesis 13 (2010) 113–130.
[24] K. Itaka, K. Yamauchi, A. Harada, K. Nakamura, H. Kawaguchi, K. Kataoka, Polyion complex micelles from plasmid DNA and poly(ethylene glycol)-poly(L-lysine) block copolymer as serum-tolerable polyplex system: physicochemical properties of micelles relevant to gene transfection efficiency, Biomaterials 24 (2003) 4495–4506.
[25] C. Patrono, Aspirin as an antiplatelet drug, N. Engl. J. Med. 330 (1994) 1287–1294.

Enhanced in vivo Magnetic Resonance Imaging of Tumors by PEGylated Iron-Oxide–Gold Core–Shell Nanoparticles with Prolonged Blood Circulation Properties[a]

Michiaki Kumagai,[†] Tridib Kumar Sarma,[†] Horacio Cabral, Sachiko Kaida, Masaki Sekino, Nicholas Herlambang, Kensuke Osada, Mitsunobu R. Kano, Nobuhiro Nishiyama, Kazunori Kataoka*

High-density poly(ethylene glycol) (PEG)-coated iron-oxide–gold core–shell nanoparticles (AuIONs) were developed as T_2-weighted magnetic resonance imaging (MRI) contrast agents for cancer imaging. The PEG-coated iron-oxide–gold core–shell nanoparticles (PEG-AuIONs) were approximately 25 nm in diameter with a narrow distribution. Biodistribution experiments in mice bearing a subcutaneous colon cancer model prepared with C26 murine colon adenocarcinoma cells showed high accumulation of the PEG-AuIONs within the tumor mass and low nonspecific accumulation in the liver and spleen, resulting in high specificity to solid tumors. T_2-weighted MR images following intravenous injection of PEG-AuIONs showed selective negative enhancement of tumor tissue in an orthotopic pancreatic cancer model prepared with Mia-PaCa-2 human pancreatic adenocarcinoma cells. These results indicate that PEG-AuIONs are a promising MRI contrast agent for diagnosis of malignant tumors, including pancreatic cancer.

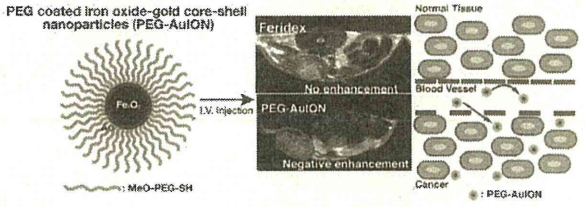

K. Kataoka, M. Kumagai, H. Cabral, S. Kaida, N. Nishiyama
Division of Clinical Biotechnology, Center for Disease Biology and Integrative Medicine, Graduate School of Medicine, The University of Tokyo, Tokyo 113-0033, Japan
Fax: +81-3-5841-7139, E-mail: kataoka@bmw.t.u-tokyo.ac.jp
K. Kataoka, T. K. Sarma, K. Osada
Department of Materials Engineering, Graduate School of Engineering, The University of Tokyo, 7-3-1 Hongo, Bunkyo-ku, Tokyo 113-8656, Japan

M. Sekino
Department of Advanced Energy, Graduate School of Frontier Science, The University of Tokyo, 5-1-5, Kashiwanoha, Kashiwa, Chiba 277-8561, Japan
N. Herlambang
Department of Mechano-Informatics, Graduate School of Information Science and Technology, The University of Tokyo, 7-3-1 Hongo, Bunkyo-ku, Tokyo 113-8656, Japan
M. R. Kano
Department of Molecular Pathology, Graduate School of Medicine, The University of Tokyo, 7-3-1 Hongo, Bunkyo-ku, Tokyo 113-0033

[a] Supporting information for this article is available at the journal's homepage at http://www.mrc-journal.de, or from the author.
[†]These authors contributed equally to the work.

Macromol. Rapid Commun. **2010**, *31*, 1521–1528

DOI: 10.1002/marc.201000341

Introduction

Pancreatic cancer is a highly aggressive cancer characterized by high invasiveness and acute resistance to chemo- and radiotherapy; consequently, it represents one of the most difficult malignancies to detect and treat.[1–2] Patient prognosis is often dismal due to late diagnosis and a lack of effective therapies. This outlook could be improved by realization of diagnostic tools useful at earlier stages of the disease.

Magnetic resonance imaging (MRI) is a powerful and noninvasive technique for medical imaging of soft tissues. MRI offers clinical feasibility for molecular imaging because it provides superb anatomic resolution and contrast for visualizing tissue morphology and anatomical details of organs in vivo.[3–6] Development of contrast agents has been central to advances in MRI techniques for early diagnosis of cancer and detection of biological processes at the cellular and molecular level. Particularly, superparamagnetic iron oxide nanoparticles are gaining popularity for MRI applications in vivo, due to their low toxicity and excellent magnetic susceptibility. These superparamagnetic iron oxide nanoparticles are extremely effective for promoting proton relaxation with significant capacity to reduce MRI signal, and this effect is further enhanced by using spin echo sequences with a longer echo time (T_2-weighted imaging).[7] Thus, the accumulation site of iron oxide nanoparticles exhibits negative enhancement of MRI signals in T_2-weighted MR images. In order to enhance the in vivo utility to include use for tumor diagnosis, iron oxide nanoparticles should be highly biocompatible, of appropriate size, and should have sufficiently long blood circulation time to allow for passive tumor accumulation through the enhanced permeability and retention (EPR) effect.[8–10] Surface modification of iron oxide nanoparticles with biocompatible polymers can avoid or effectively reduce recognition by the reticuloendothelial system (RES), thus improving their circulating properties.

Poly(ethylene glycol) (PEG) has found widespread clinical use as a biocompatible, nonspecific protein resistant material that prolongs the circulation time of protein therapeutics.[11–12] PEG-based block copolymers and PEGylated liposomes have been used to improve the stability and pharmacokinetics of iron oxide nanoparticles in the physiological environment.[13–14] Many groups showed negative enhancement at the hypervascular tumor site in tumor-bearing mice using PEG-coated iron oxide nanoparticles and T_2-weighted MR imaging.[15–16] We also reported PEG-coated iron oxide nanoparticles with a hydrodynamic diameter of ≈100 nm as a negative contrast agent for successful MR imaging of subcutaneous colon tumor models.[17] However, there are no reports to enhance the MR imaging of pancreatic tumors using PEG-coated iron oxide nanoparticles without targetable biomolecules, because PEG-coated iron oxide nanoparticles developed to date have limited circulation in the blood compartment and are too large to penetrate into pancreatic tumors. In fact, without intraperitoneal administration of transforming growth factor-β (TGF-β) inhibitor, PEG-coated iron oxide nanoparticles (≈100 nm) failed to accumulate into a subcutaneous BxPC3 pancreatic tumor model, which is characterized by hypovascularity and thick fibrosis.[18] We have recently found that the size upper limit of the nanoparticle system for passive targeting to pancreatic tumor models is ≈50 nm (unpublished data). Hence, we hypothesized that with proper control of the size and surface properties of iron oxide based nanoparticles, development of effective T_2-weighted MRI contrast agents for in vivo detection of pancreatic tumors could be possible.

Recently, gold-coated superparamagnetic core–shell nanoparticles have attracted considerable attention for biomedical applications.[19–23] Au and iron oxide nanoparticles are known to be biocompatible and have been used extensively for optical- and magnetic-based applications, respectively.[24–25] Furthermore, a gold coating on the magnetic nanoparticles is stable under biological conditions and can be further functionalized with sulfur-containing moieties through Au–S bonding.

In this report, we developed PEG-coated iron-oxide–gold core–shell nanoparticles (PEG-AuIONs) for use as a T_2-weighted MRI contrast agent for imaging of pancreatic tumor models. In our method, the overall size of the nanoparticle was controlled by coating iron oxide nanoparticles with Au that allowed for reaction with methoxy-PEG-thiol (MeO-PEG-SH) and subsequent formation of a high-density PEG coating on the surface through Au–S bonding, without the formation of any higher-order assemblies. Our results demonstrated that PEG-AuIONs showed prolonged blood circulation and enhanced MR imaging of subcutaneous colon and orthotopic pancreatic tumor models. These findings suggest that our method, which allows precise control of hydrodynamic size and effective PEG density on the iron-oxide–gold core–shell nanoparticle (AuION), could be a promising method for development of MRI contrast agents for various tumor types including pancreatic cancer.

Experimental Part

AuION was synthesized with a slight modification of a previously reported method.[20,26] Hydrogen tetrachloroaurate was reduced by oleylamine to form a thin gold layer onto oleylamine and oleic acid stabilized iron oxide nanoparticles. MeO-PEG-SH ($\overline{M}_w$: 2 000) was introduced onto the surface of AuIONs through a sequential coating process in chloroform and then in methanol, followed by a solvent exchange to water. Details of PEG-AuION synthesis and characterization are provided in the Supporting Information (SI). The biodistribution of PEG-AuIONs, including tumor accumulation, was evaluated in tumor-bearing mice by measuring the Au content in blood and tissues using inductively coupled plasma–mass spectrometry (ICP-MS). In vivo MRI was performed using a 4.7 T scanner with mice bearing a subcutaneous colon (C26) or

Macromol. Rapid Commun. 2010, 31, 1521–1528

Macromolecular Journals
DOI: 10.1002/marc.201000341

orthotopic pancreatic (MiaPaCa) tumor. All the details regarding physicochemical and biological studies are provided as SI.

Results and Discussion

Synthesis of PEG-Coated Iron-Oxide–Gold Core–Shell Nanoparticles (AuION)

Figure 1a shows the schematic representation for preparation of the PEG-AuIONs used in this study. First, nearly monodispersed γ-Fe_2O_3 nanoparticles with an average diameter of 10.5 ± 1.6 nm were obtained by thermal decomposition of $Fe(CO)_5$ in the presence of the capping agents oleylamine and oleic acid (5:1), under aerobic conditions with a slight modification of a previously reported method.[26] A small amount of oleic acid was added into the reaction mixture to avoid the formation of γ-Fe_2O_3 nanoparticles with different shapes. In the next step, Au was coated onto the γ-Fe_2O_3 nanoparticle surface by the reduction of $HAuCl_4$ with oleylamine at 140 °C in

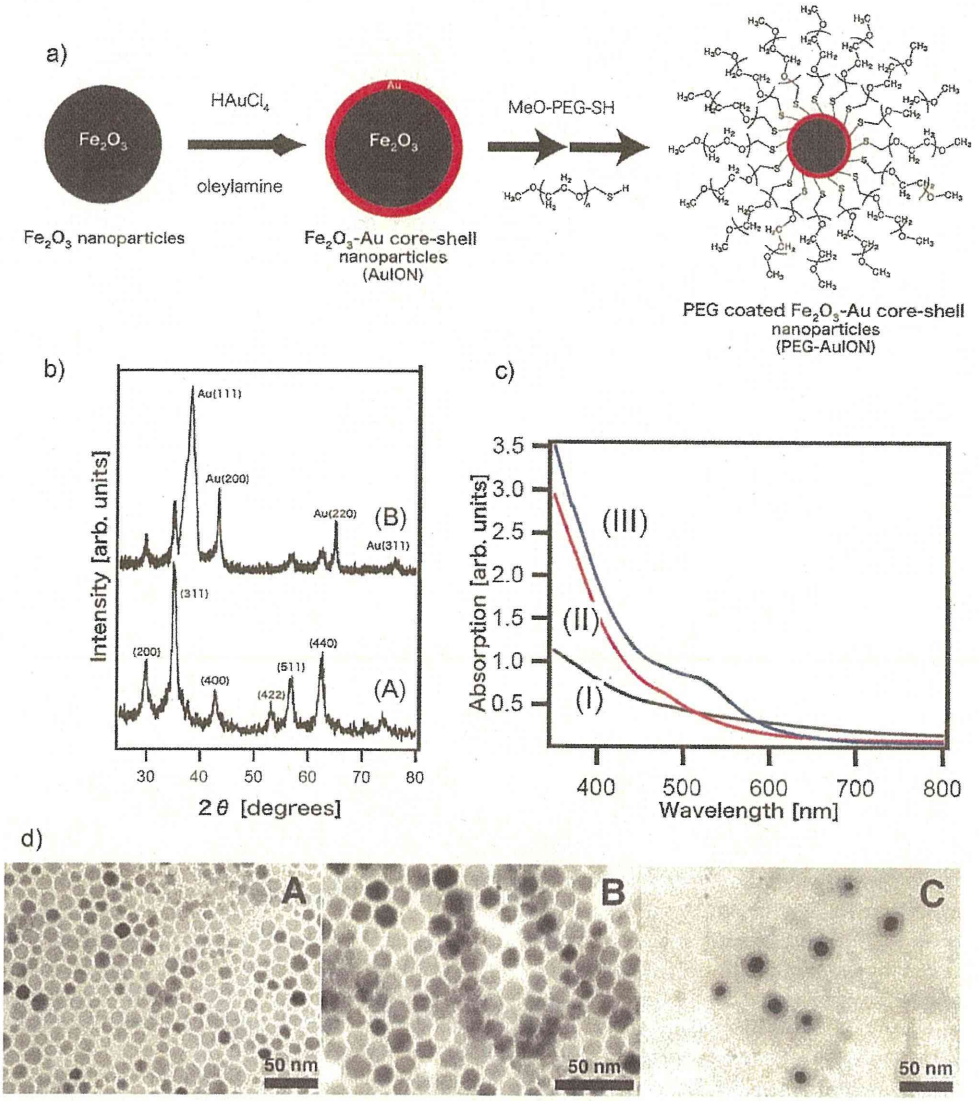

Figure 1. Preparation and properties of PEG-AuIONs. a) Scheme for Au shell formation onto γ-Fe_2O_3 nanoparticles and subsequent coating with MeO-PEG-SH to form biocompatible PEG-AuIONs. b) X-ray diffraction pattern of γ-Fe_2O_3 nanoparticles (A) and AuIONs (B); the Braggs's reflections for both nanoparticles are shown. c) UV–visible spectra of I) γ-Fe_2O_3 nanoparticles in chloroform, II) AuIONs in chloroform, and III) PEG-AuIONs in aqueous medium. d) Transmission electron microscopy images of A) γ-Fe_2O_3 nanoparticles, B) AuIONs in chloroform, and C) PEG-AuIONs in aqueous medium. The PEG layer is visible on the AuION surface in C. The nanoparticles were stained with 1% phosphotungstic acid solution. The scale bar represents 50 nm in all TEM images.

1,2-dichlorobenzene (ODCB), where oleylamine functions as both the reducing agent and the stabilizer.[21] Oleylamine coated AuIONs were washed by several cycles of dispersion-centrifugation to remove excess oleylamine, and were finally dispersed into chloroform for further modification.

The formation of an Au shell on the γ-Fe_2O_3 nanoparticles was confirmed by X-ray diffraction measurement as shown in Figure 1b. Evolution of Bragg's diffraction peaks from the face-centered cubic (fcc) lattice structure of Au are clearly visible from the X-ray diffraction spectra of AuIONs. Using the Debye–Scherer equation, the thickness of Au on the γ-Fe_2O_3 surface was calculated to be 1.3 nm. Transmission electron microscopy (TEM) studies (Figure 1d(A,B)) showed that the average particle size increased by 1.5 ± 0.6 nm following Au deposition onto the γ-Fe_2O_3 nanoparticles, which is comparable to the thickness of Au calculated from the X-ray diffraction peaks.

PEG was readily conjugated to the particle surface by reaction of PEG-SH with the gold surface through well-known thiol–gold coupling chemistry. After a single cycle of PEG modification, followed by the evaporation of chloroform under vacuum, PEG-AuIONs were readily soluble in aqueous medium. However, when the nanoparticles were incubated for 12 h in 150×10^{-3} M NaCl solution, agglomeration occurred, suggesting incomplete coating of MeO-PEG-SH on the nanoparticle surface (data not shown). Therefore, repetitive PEG coating onto PEG-AuIONs (described in SI) was performed to increase the PEG density on the particle surface, as it has been reported that the process involving repetitive PEG adsorption significantly contributes to increase the PEG density on the gold surface.[27] Salt-induced agglomeration of PEG-AuIONs obtained by this double PEG coating process was avoided, even after transfer into aqueous media through dialysis, suggesting the formation of a PEG layer with appreciably high density around the AuION surface. PEG-AuIONs stored in 10×10^{-3} M Tris-HCl buffer containing 0.03% bovine serum albumin were stable for several months without any notable aggregation. Use of methanol as the solvent for the second cycle of PEG coating also proved to be crucial for controlling particle size and dispersity of the PEGylated nanoparticles, as application of the second PEG coating onto the AuIONs in water resulted in low quality particles with large hydrodynamic diameter and high polydispersity index (data not shown).

The formation of an Au shell on the γ-Fe_2O_3 surface was further confirmed by UV–vis spectroscopy of the PEG-AuION in aqueous medium. As shown in Figure 1c, AuIONs did not show any characteristic plasmon resonance in organic medium as AuIONs are protected by the long chain alkyl ligands. However, when the AuION was transferred to the aqueous medium as a PEGylated nanoparticle, a plasmon resonance band appears with absorption at 515 nm, probably due to the increased dielectric constant of the medium.

Characterization of PEG-Coated Iron-Oxide–Gold Core–Shell Nanoparticles (PEG-AuION)

The TEM image of PEG-AuION transferred to water after surface modification with MeO-PEG-SH (Figure 1d(C)) showed no apparent agglomeration. Furthermore, the PEG layer surrounding the AuION core was visible in TEM after negative staining with 1% phosphotungstic acid as seen in Figure 1d(C). The thickness of the PEG layer was determined to be 6.5 ± 1.2 nm from this TEM image.

The neutral ζ-potential of 0.49 ± 0.12 mV of PEG-AuIONs in water showed complete passivation of the nanoparticle surface with the PEG layer. The number of PEG molecules (molecular weight = 2 kDa) on the surface of a single 12.9 nm AuION was calculated to be ~2500 by thermogravimetric analysis (TGA) analysis of the sample under N_2 atmosphere. This surface coverage corresponds to a footprint area of 0.25 nm^2 per PEG molecule, which is significantly smaller than previous reports for MeO-PEG-SH conjugated on Au nanoparticle surfaces (2.42 nm^2).[28–29] This result suggests that the PEG-AuION possesses an appreciably dense PEG layer. Chain conformation of grafted PEG on a surface plane is estimated to be an extended brush at this density (0.25 nm^2). Nevertheless, on a spherical surface, PEG density decreases in a radial direction toward the exterior of the particle with a change in the PEG conformation from brush to random coil (a mushroom model).[30] Note that the height of PEG 2kDa in a mushroom conformation is estimated to be 3.3 nm (twice of radius of gyration (R_g)) as lower limit,[31] whereas the height in an extended conformation is estimated to be 15.9 nm as upper limit by using the effective monomer length of PEG in water ($2000/44 \times 0.35 = 15.9$ nm).[32] The PEG thickness estimated from the TEM image for PEG-AuIONs obtained in this study (6.5 ± 1.2 nm) is in the range between these lower and upper estimated heights of PEG in the extended brush and random coil conformation.

The dispersion stability of PEG-AuIONs against increased NaCl concentration in aqueous solution was evaluated by dynamic light scattering (DLS) measurement, which revealed that the hydrodynamic diameter remained constant up to 1 M NaCl (Figure 2a). Furthermore, there was no change in the diameter of PEG-AuIONs even after 12 h incubation in 10×10^{-3} M Tris-HCl buffer containing 10% fetal bovine serum at pH 7.4 and 37 °C (Figure 2b). PEG-AuIONs were also found to be stable in buffer within the pH range of 3–10.

To examine the feasibility of PEG-AuIONs as a T_2–weighted MRI contrast agent, we evaluated the relaxivity r_2 of PEG-AuIONs and determined the value to be $149.32 \times 10^{-3}\ M^{-1} \cdot s^{-1}$ (Figure 2c). This r_2 value is comparable to the commercially

Macromol. Rapid Commun. 2010, 31, 1521–1528

DOI: 10.1002/marc.201000341

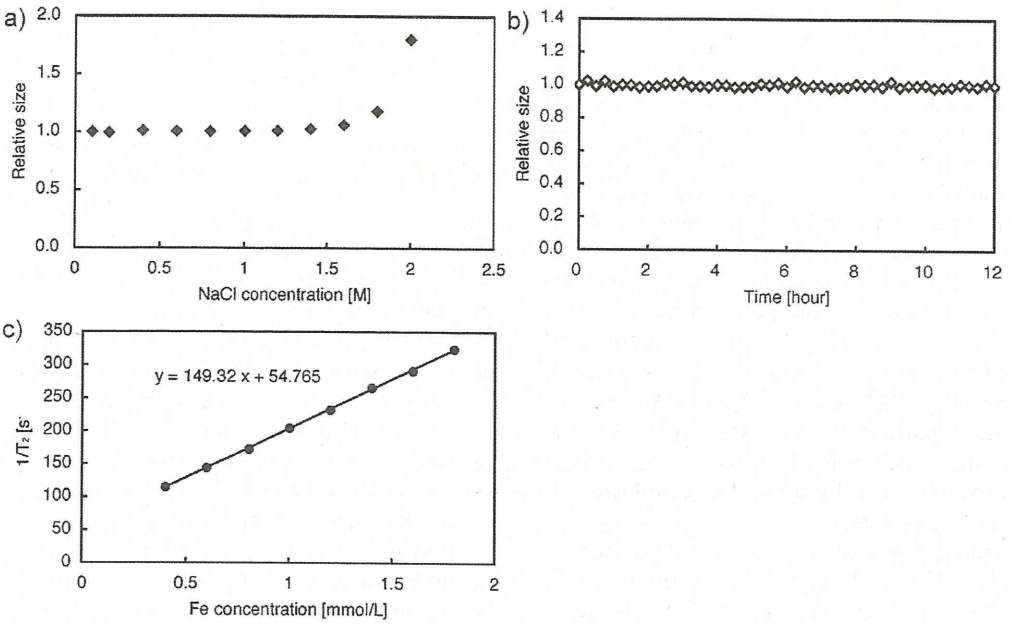

Figure 2. a) Change in the relative particle size of PEG-AuIONs with increased NaCl concentration, determined by DLS measurement. b) Time-dependency of the relative size of PEG-AuIONs in Tris-HCl buffer containing 10% fetal bovine serum at 37 °C. c) Relaxivity r_2 of PEG-AuIONs using the Carr-Purcell-Meiboom-Gill (CPMG) pulse sequence at 25 °C, 0.59 T.

available T_2 contrast agent Feridex (dextran-coated iron oxide nanoparticles).

Biodistribution of PEGylated Fe_2O_3-Au Core–Shell Nanoparticles

Figure 3 shows the concentration of gold in blood plasma over time after intravenous administration of PEG-AuIONs. The gold concentration measured in plasma indicates that PEG-AuIONs stably circulate in the blood compartment with 8% of the injected dose observed even after 24 h. Prolonged blood circulation of the PEG-AuION was reasonably associated with high stability of PEG-AuIONs under physiological conditions at 37 °C (Figure 2). Accumulation of PEG-AuIONs within solid tumor and normal tissues (liver, kidney, spleen and muscle) is also shown in Figure 3. Notably, PEG-AuION showed continuous accumulation with time into solid tumors, while its accumulation to other tissues was somewhat limited.

To assess the selectivity towards the solid tumors, the area under the Au concentration–time curve (AUC) and AUC ratios of the tumor to normal tissues at 24 h after injection were determined and are shown in Supplementary Table 1 in the SI. PEG-AuIONs exhibited ratios $AUC_{tumor}/AUC_{organ} > 1.0$ for spleen, kidney, and muscle tissues, indicating selectivity to the tumor (AUC_{tumor}/AUC_{organ} of 2.84, 1.21, and 67.27 for spleen, kidney, and muscle tissues, respectively). These AUC_{tumor}/AUC_{organ} ratios are comparable to those observed for so-called stealth drug carriers.[33] However, AUC_{tumor}/AUC_{liver} ratio is somewhat low at 0.95. This may be due to the relatively high blood volume in the liver. Note that liver has about one-fifth of blood volume in the body, and the liver accumulation value for PEG-AuIONs has a substantial contribution from PEG-AuIONs present in the blood pool.

In vivo Tumor Imaging

In order to study the efficacy of PEG-AuIONs for dynamic in vivo MRI, imaging of tumor tissue was conducted and compared with the commercially available MRI contrast agent Feridex (dextran-coated iron oxide nanoparticles). First, we performed in vivo MRI with nude mice bearing subcutaneously inoculated murine colon adenocarcinoma (C26) cells (Figure 4a,b). Negative enhancement of the tumor site in T_2-weighted images, which is indicated as circled by red line in Figure 4, gradually increased 5 min after injection of PEG-AuIONs, with a maximum negative enhancement of 60% observed at 4 h post-injection (Figure 4a,e and Table 1). Note that MRI signals in other organs and tissues surrounding the tumor were also negatively enhanced in T_2-weighted images due to the existence of high concentration of PEG-AuIONs in the blood circulation. Therefore, the percentile rates of negative enhancement at 4 h post-injection of PEG-AuIONs were compared between in the tumor and the intestine